Department of Construction Sciences
Solid Mechanics

ISRN LUTFD2/TFHF-21/5245-SE(1-77)

Continuum damage modeling of delamination in paperboard
For creasing and folding

Master's Dissertation by

Erik Jacobsson

Supervisors:
Eric Borgqvist, PhD. Tetra Pak Packaging Solutions AB
Kristofer Robertsson, PhD student. Divison of Solid Mechanics

Examiner:
Mathias Wallin, Professor. Divison of Solid Mechanics

Printed by Media-Tryck AB, Lund, Sweden
For information, address:
Division of Solid Mechanics, Lund University, Box 118, SE-221 00 Lund, Sweden
Webpage: www.solid.lth.se

Preface

This master thesis was conducted as a collaboration between Tetra Pak and the Division of Solid Mechanics at Lund University.

I acknowledge with gratitude the help I have received from my supervisors Eric Borgqvist and Kristofer Robertsson, who have supported me and answered all my questions from start to finish. I also wish to thank Mikael Schill at Dynamore, not only for being patient when helping me through my difficulties concerning the simulation modeling, but also for the general support and positive feedback. I would also like to thank Anders Bernhardsson, who helped me a lot with the simulation modeling in LS-Dyna. Furthermore, I wish to thank Peter Johannesson for all the support and creative thoughts about modeling issues and simulation. Finally, I would like to thank Johan Tryding for giving me insight in paper mechanics and for all the constructive feedback throughout my work.

Lund, June 2021

Erik Jacobsson

Abstract

This work concerns the creasing and folding of a continuum paperboard material model developed by Borgqvist et al. (2014). Creasing is an operation that induces permanent deformation in the material, undertaken for the folding to be performed along a straight fold line without any in-plane cracks. The material model concerned is complex and involves a high degree of anisotropy, and it has earlier been proven to be able to predict many of the material behaviours observed during experimental testing. However, not all test setups are predicted accurately. One such setup is the folding of creased paperboard. This issue is considered in this work.

To give a short background of the concerned problem, it is stated that the paperboard is an anisotropic material which, in a simplified manner, can be viewed as possessing three fundamental material directions. The creasing and folding operations can be undertaken in both in-plane directions of the paperboard, which are called the MD- and CD-direction, respectively. It has earlier been observed that the material model quite well predicts the creasing and folding of uncreased paperboard. However, for the folding of creased paperboard, the material model does not predict the response in a sufficiently satisfying manner - the response is too stiff.

The scope of this work is to investigate if the folding of creased paperboard in the MD-direction can be predicted more accurately by including damage in the material model. The creasing and folding operations are simulated by using the commercial engineering software LS-Dyna, which is an advanced general-purpose simulation software. The introduction of damage is made as an add-on feature to the continuum material model via an LS-Dyna built-in software called eGISSMO. Damage is thus introduced on top of the existing material model.

The results in this thesis show that, by introducing damage in LS-Dyna, it is possible to accurately predict the folding response of MD creased paperboard.

Keywords: *Creasing, Folding, MD-direction, EB material model, LS-Dyna, eGISSMO.*

Contents

1 Introduction

Paperboard is a material that is widely used in the packaging industry. In general, the paper-based package consists of paperboard as well as metallic and polymer films. In the package, paperboard is the bulk material, taking up the largest volume and providing the most stiffness. In the industrial process, in which the package is manufactured, the material undergoes several processing steps. In general, paperboard is a material that is suitable for different converting operations, cf. Calvin (1988). Two converting operations that are of importance are the *creasing* and *folding* operation. The creasing operation takes place before the folding of the package in order for the package to obtain straight fold lines without in-plane cracks, cf. Borgqvist (2016).

Each year, several hundred billion packages are produced. To reduce the amount of waste produced during manufacturing, it is of importance that the converting operations are undertaken in a controlled manner. To achieve this, knowledge of the paperboard material and its mechanical properties is crucial. One way to estimate and determine the mechanical behaviour of the paperboard is to carry out extensive experimental testing. This method can be sufficient for controlling procedures and for checking the quality of the paperboard before entering the large-scale industrial application. However, such a method cannot entirely capture the behaviour of the paperboard during the converting process. Hence, other methods are needed. One such other method is to develop mathematical constitutive models of the paperboard. With such models at hand, the effects of the converting operations can be predicted by the use of numerical simulations. The simulations can provide information about the variation and size of local deformation, properties that are hard to obtain from experimental testing. With this understanding, the converting process can be improved and optimized, resulting in less waste produced and a more effective overall packaging process.

In recent years, several constitutive continuum models of paperboard have been developed. Authors common in the literature are for example Xia et al. (2002), who also underlines that, considering the fact that paper has existed since ancient China, the amount of constitutive models available to describe the mechanical behaviour is still rather limited. In this thesis, the constitutive continuum material model developed by Borgqvist (2016) is considered. The model, which in the following will be referred to as the *EB material model*, has shown promising results.

However, it cannot sufficiently accurately predict the material response of the folding of paperboard creased in a certain material direction called the MD-direction. The predicted response is stiffer than what is observed by experiments. In this thesis, the issue of obtaining a better prediction of this folding operation is considered. To do this, damage is introduced in the material model.

The creasing and folding operations are simulated by using the commercial engineering software LS-Dyna, which is an advanced general-purpose simulation software. The introduction of damage is made as an add-on feature to the continuum material model via a built-in software in LS-Dyna called eGISSMO.

The thesis is structured in five sections, namely theory, simulation without damage, simulation with damage, uniaxial tests, and conclusion. In the theory section, the basic properties of the paperboard, as well as the EB material model and the damage model, is described. Next, the simulation setup of the creasing and folding operations as well as the simulations results, without any incorporation of damage, is presented. After

this, the same converting operations with damage included. After this, uniaxial ZD-tension and MDZD-shear tests in the out-of-plane direction are simulated. Finally, the results are evaluated in the conclusion section.

2 Theory

In this section, some basic aspects of the paperboard material, as well as the EB material model, are considered. First, in section 2.1, some basic properties of the paperboard material are described, such as the manufacturing process and some uniaxial mechanical properties. Next, in section 2.2, the line creasing method and the line folding method is described. After this, a summary of the elastic and plastic properties of the EB material model is provided in section 2.3. Finally, the damage model used to calibrate the response is explained in section 2.4.

2.1 The paperboard material

In this section, two subsections considering the paperboard material is provided. First, the general structure of the paperboard, and how it is manufactured, is described. This is done in section 2.1.1. After this, some basic mechanical properties of the material, that are of importance for the upcoming damage calibration, are highlighted. This is done in section 2.1.2.

2.1.1 Manufacturing process

Paperboard is a highly anisotropic material. The inherent anisotropy comes from the manufacturing process, in which fibres, which is mainly cellulose fibres, are sprayed on top of a rolling web. Apart from cellulose fibres, the paperboard material consists of starch and other chemicals. The density of paperboard used in packages is commonly about 300-900 kg/m^3, and the thickness ranges from 0.2 mm to 0.5 mm. Moreover, the paperboard can be manufactured either as a single ply or as a composite of multiple plies. In the multiple ply paperboard, each layer is completely distinct and can have a specific thickness and fibre orientation. Analogous with the concept of an I-beam, the stiffness is often distributed towards the edges of the ply. In this work, a homogeneous paperboard with a single ply is assumed.

Due to the manufacturing process, the fibres arrange in planes stacked on top of each other in the out-of-plane direction. The orientation of the fibres depending on the number of fibres sprayed, the fibre deposition speed and the thickness and length of the individual fibres. The rolling direction is in the industry called the machine direction (MD). The majority of the fibres aligns parallel with this direction. The direction perpendicular to the MD-direction, and in the same plane, is called the cross direction (CD). The third direction is called the out-of-plane direction, or the ZD-direction. The described coordinate system is depicted in Fig. 1.

As described above, due to the manufacturing process, the fibres align in a way that gives the paperboard clear anisotropic properties. The paperboard can in a simplified manner be viewed as an orthotropic material, i.e. as a material with three distinguished material directions. The stiffness in the MD-direction is about 2-3 times higher than the stiffness in the CD-direction and about 100 times higher than the stiffness in the ZD-direction. The mechanical properties are further explained in the next section.

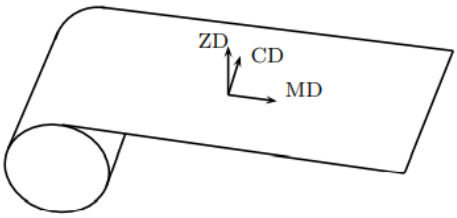

Figure 1: Material directions of the paperboard. The directions, which are a consequence of the manufacturing process, are called the Machine Direction (MD), Cross Direction (CD) and the ZD-direction.

2.1.2 Mechanical properties

To underline the already mentioned high anisotropy of the paperboard, in-plane uniaxial tensile tests are considered. In Fig. 2 uniaxial tests in the MD-, CD- and 45 degrees direction is shown. It is noted that the paperboard has a higher stiffness and a higher tensile strength but a lower failure strain in the MD-direction compared with the CD-direction.

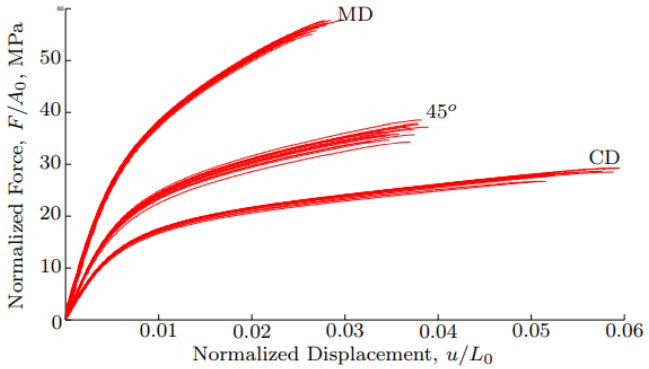

Figure 2: Experimental in-plane uniaxial tension test of the paperboard material. Note that the strength in the MD direction is significantly higher than the strength in the CD direction. Source: Borgqvist (2016).

Considering instead in-plane compression tests, it is noted that these are more difficult to carry out than tensile tests since stability in this case becomes an issue, refer to Borgqvist (2016). Two compression test methods are the Short Compression Test (SCT), in which the span length is 0.7 mm, and the long edge test, in which a 55 mm long paperboard is tested. The SCT test follows the ISO standard, cf. ISO:9895:2008 (2008). The described methods differ in the sense that the measured strengths are all higher in the SCT compared with the long edge test. However, in both methods, the MD-test exhibit a higher compression strength than the CD-test.

Regarding the out-of-plane testing, the difficulty of carrying out the tests is, in theory, opposite to the in-plane situation, i.e. compression tests are more easily carried out than tension tests. However, practically this is not the case, since it is in the out-of-plane compression test difficult to arrange the plates completely parallel to each other. The tension test is carried out by gluing metal blocks to the paper material, refer to

Nygårds (2008). For the compression tests, paperboard hysteresis with permanent deformations can be observed in the force-displacement curve. This hysteresis is also observed in the tension tests, refer to Fig. 3. For the tension test, a clear softening behaviour is observed in the material.

In Fig. 4, an out-of-plane shear test is shown. Also for this test, a softening in the material is observed. It should however be noted that out-of-plane shear tests are difficult to carry out, which usually leads to large variations in the obtained experimental results.

The material behaviour due to out-of-plane tension and shear in Figs. 3 and 4 is highlighted since these two deformation mechanisms are used in the upcoming damage calibration.

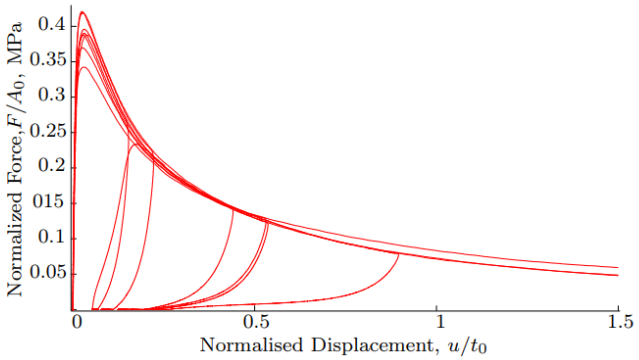

Figure 3: Experimental out-of-plane uniaxial tension test of the paperboard material. Source: Borgqvist (2016).

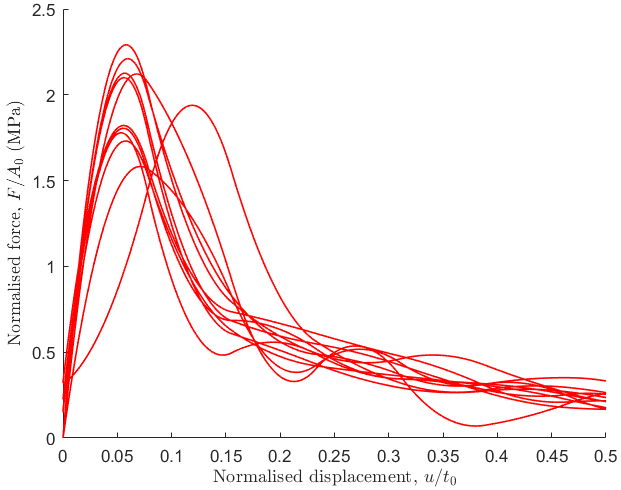

Figure 4: Experimental out-of-plane shear test of the paperboard material. Source: Biel et al. (2020).

2.2 Converting operations

The converting operations considered in the implementation of the new continuum damage model are the creasing and folding operations. As previously mentioned, the creasing operation is undertaken in order for the package to be folded without unwanted defects.

2.2.1 Creasing

The creasing operation is a process that introduces local damage into the paperboard, cf. Borgqvist (2016). Hence, this converting procedure is critical when studying the effects of the implementation of damage. Due to the introduced damage, the bending stiffness of the material is reduced. Thus, the folding of the material will, preferably, take place in the creased region, which is exactly what is desired.

When forming packages in the industry, a rotational creasing operation is undertaken with two cylindrical dies. The paperboard is placed between the dies, which are then rotated such that one of them, the male die, is pressed into the grooves of the other die, the female die. The creasing pattern is, in the general case, two-dimensional and, as such, this allows for the creation of the creasing lines needed to fold the package along.

A simplified creasing method, that is used in the industry to control the quality of the paperboard, is the *line creasing method*. Using this setup, different effects such as crease speed, crease depth and tool geometry can be isolated. The setup is illustrated in Fig. 5. In contrast to the above-explained rotational creasing setup, the creasing pattern is in the line creasing two-dimensional, i.e. a straight line. The process is similar to the three-dimensional case - the paperboard is placed in between the male and female die and the male die then press the paperboard into the grooves of the female die. To consider the effect of web tension, the paperboard is given an initial prescribed displacement u_w which is held constant during the creasing operation. Note in Fig. 5 that the x-axis is denoted as CD/MD. This means that both the MD- or CD-direction may be aligned with the x-axis.

The deformed configuration of the paperboard during the line creasing method is illustrated in Fig. 6. It is emphasized that, in particular, out-of-plane shear and tension strains are introduced in the paperboard along the creasing line.

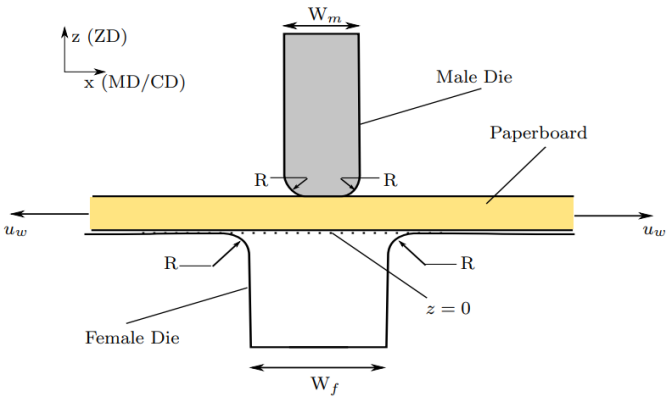

Figure 5: Principal sketch of the line creasing operation. Source: Borgqvist (2016).

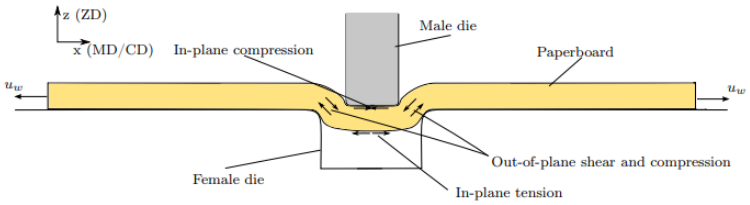

Figure 6: Principal sketch of the deformed configuration during the line creasing operation. Source: Borgqvist (2016).

2.2.2 Folding

The simplified folding setup, corresponding with the line creasing operation, is the *line folding operation*. In this setup, the paperboard is clamped along a certain length by two clamps, pressing on both sides of the paperboard. After the two clamps have achieved the chosen pressure, they are rotated 90 degrees. Thus, the paperboard is folded. However, to fold the paperboard during the rotation, a rigid support must be provided. This rigid support is a load cell placed with a certain distance l_o from the ends of the clamps. A schematic illustration of the line folding setup is presented in Figs. 7 and 8. The difference between these two figures is that the paperboard is uncreased in Fig. 7, whereas it is creased in Fig. 8.

For uncreased paperboard, there is an uncertainty of the location at which the folding will take place. As depicted in Fig. 7, the rotation will induce a wrinkle in the paperboard. The wrinkle is a consequence of the high compressive stresses that form in the bottom of the paperboard during the rotation of the clamps. As underlined in section 2.1.2, and in particular showed in Fig. 2, the paperboard has a lower strength in compression compared with tension. Hence, the wrinkle forms on the compressed side of the paperboard.

For creased paperboard, local damage has been introduced in the previously undertaken creasing operation along what is called the creasing line. Along the creasing line, the bending strength of the paperboard is reduced. Thus, the creasing line will therefore act as a plastic hinge during folding. Furthermore, the paperboard will, as the bending angle increases, be separated along the creasing line, cf. Borgqvist (2016). This separation process is called delamination, refer to Fig. 8. It has been observed that two important deformation modes during folding of creased paperboard is the out-of-plane shear and tension. To give an illustration of the deformation pattern, the folding of creased paperboard during an experimental test is depicted for different bending angles in Fig. 9.

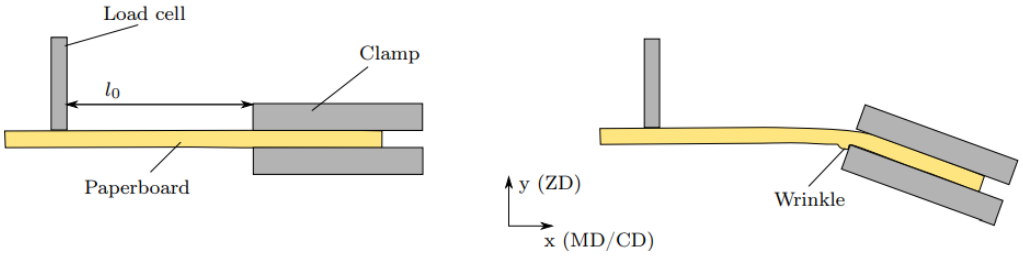

Figure 7: Principal sketch of the line folding operation. The paperboard is uncreased. Source: Borgqvist (2016).

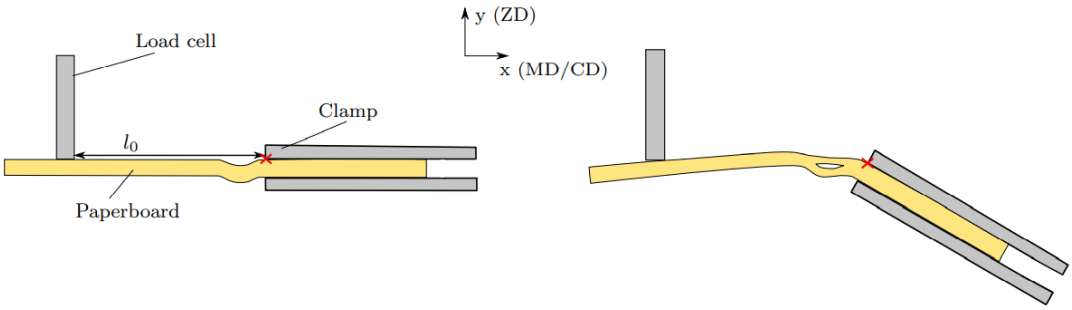

Figure 8: Principal sketch of the line folding operation. The paperboard is creased. Source: Borgqvist (2016).

(a) Bending angle approximately 10 degrees.

(b) Bending angle approximately 20 degrees.

(c) Bending angle approximately 60 degrees.

Figure 9: Folding of creased paperboard at different bending angles. Source: Borgqvist (2016).

Finally, in Fig. 10 two experimental data sets of the folding of creased and uncreased paperboard are depicted. It is observed that the response is quite different for the two cases. Hence, it is concluded that the extent of creasing has a large effect on the folding response. In the industry, different measures exist to identify the quality of the paperboard in terms of the crease and foldability. One common measure is the *Relative Crease Strength* (RCS), which is defined as the ratio between the maximal moment in creased and uncreased paperboard

$$\text{RCS} = \frac{M^{max}_{b,creased}}{M^{max}_{b,uncreased}},$$

refer to Coffin and Nygårds (2017). The bending moment is calculated as $M_b = Pl_o$, where P is the reaction force at the load cell and l_o is the distance between the load cell and the center of rotation. Thus, the above expression can equally be written as

$$\text{RCS} = \frac{P^{max}_{b,creased}}{P^{max}_{b,uncreased}}.$$

At Tetra Pak, the RCS is for package materials commonly measured as the maximal force between 0 and 30 degrees of bending

$$\text{RCS} = \frac{P^{max}_{b,creased,0<\theta<30}}{P^{max}_{b,uncreased,0<\theta<30}},$$

which also is the measure used in this work. By evaluating Fig. 10, the RCS is calculated as

$$\text{RCS} = \frac{1.95}{5.05} = 0.39.$$

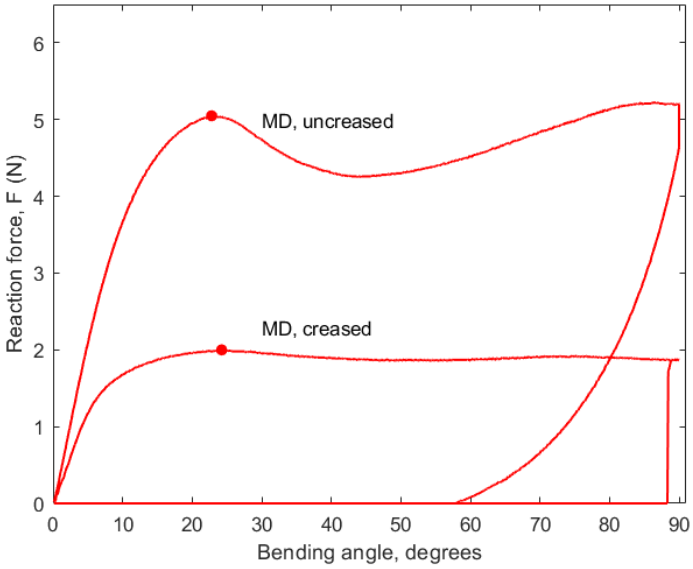

Figure 10: Reaction force at load cell vs. bending angle for creased and uncreased paperboard in the MD-direction. The maximal forces between 0 and 30 degrees of bending are marked with red circles.

2.3 The EB material model

In this section, the constitutive material model developed by Borgqvist et al. (2014) is explained in some detail. First, the modeling assumptions are clarified in section 2.3.1. Next, in section 2.3.2, the notation convention is explained. Finally, a description of the elastic and plastic behaviour is provided, refer to sections 2.3.3 and 2.3.4. The derivations build on the basic principles of kinematics for large deformations and the basic principles of thermodynamics. These principles are explained in appendix 7.1, in which also the specification of the free energy as well as the full derivation of the stress tensor is provided.

2.3.1 Modelling assumptions

As mentioned in the introduction, it has been proven that continuum material models, to some extent, can predict the mechanical behaviour of the paperboard material. To start with, it is mentioned that it has been shown that plastic strains develop in the paperboard material when unloaded, refer to e.g. Harrysson and Ristinmaa (2008). As previously mentioned, the paperboard is highly anisotropic. Furthermore, large deformations take place during the converting operations. Hence, an anisotropic large strain plasticity model is needed to capture the behaviour of the material.

The characteristic of the material is also highly dependent on outer climate factors such as moisture content and temperature. Furthermore, paperboard is not a homogeneous material concerning the ZD-direction, neither is it unaffected by damage, rate

of loading, creep or large deformations. Many of these effects come into play during the creasing and folding operation. However, since material modelling always is a balance between computational cost and accuracy, only a few of these effects have been considered in the EB material model. As all converting operations is supposed to take place in a climate-controlled environment, a moisture and temperature independent model was assumed. Furthermore, the model was assumed to be rate-independent and without the inclusion of any damage. The assumptions and choices used to build the material model is summarized in Table 1.

Table 1: An overview of the characteristic properties of the paperboard material. Properties included in the considered version of the EB material model is marked with an x. Note that the material model can in fact be changed so that it is calibrated also for some other properties, such as temperature and moisture content.

Anisotropy	x
Plasticity	x
Large strains	x
Heterogeneity in ZD	
Rate-dependency	
Creep	
Moisture	
Temperature	
Damage	

2.3.2 Notation convention

The notation convention in this report follows the standard notation convention used in the literature, cf. Holzapfel (2000). Both index notation and tensor notation is used. Lowercase Greek letters (α, β, γ) are used to denote scalars, whereas lowercase boldface Latin letters $(\boldsymbol{a}, \boldsymbol{b}, \boldsymbol{c})$ are used to denote first-order tensors. Second-order tensors are in general denoted by uppercase letters $(\boldsymbol{A}, \boldsymbol{B}, \boldsymbol{C})$. However, second-order tensors are in some cases also denoted by lowercase letters. This depends on the configuration considered. For tensors defined in the reference (Lagrangian) configuration, uppercase letters $(\boldsymbol{M}^{(1)}, \boldsymbol{M}^{(1)}, \boldsymbol{M}^{(1)})$ are used, whereas tensors defined in the current (Eulerian) configuration, lowercase letters $(\boldsymbol{m}^{(1)}, \boldsymbol{m}^{(2)}, \boldsymbol{m}^{(3)})$ are used. For an explanation of the concept of different configurations, the reader is referred to appendix 7.1.

2.3.3 Elasticity

In this section, the specific choice of the Helmholz free energy is presented. The energy is split into an elastic and a plastic part. Provided a suitable elastic energy the stress state can be calculated from the dissipation inequality using thermodynamical arguments. The reader is referred to appendix 7.1 for further details. In the EB material model, the elastic part is split into one part related to the in-plane properties and another part related to the out-of-plane properties

$$\rho_o \psi^e = \rho_o \psi^{e_{ip}} + \rho_o \psi^{e_{op}}. \tag{1}$$

The invariants describing the model are chosen as

$$I_{11} = \sqrt{\boldsymbol{m}^{(1)} : \boldsymbol{I}}, \quad I_{12} = \sqrt{\boldsymbol{m}^{(2)} : \boldsymbol{I}}, \quad I_{13} = \sqrt{\boldsymbol{m}^{(3)} : \boldsymbol{b}^e\boldsymbol{b}^e},$$
$$I_{23} = \sqrt{\boldsymbol{m}^{(3)} : \boldsymbol{I}}, \quad J^e = \sqrt{\det \boldsymbol{b}^e}.$$

where $\boldsymbol{b}^e$ is the elastic Finger's deformation tensor and $\boldsymbol{m}^{(\alpha)}$ are the structural tensors, refer to (27) and (34) in appendix 7.1, respectively. As showed by Borgqvist (2016), the invariants I_{11}, I_{12} and I_{13} can be interpreted as the stretch in the MD, CD and ZD direction, respectively. Moreover, the invariants I_{23} and J^{e} can be interpreted as the stretch of the area and volume element, respectively. The in-plane part of the elastic energy is chosen as

$$\rho_o\psi^{e_{ip}} = A_1\Big(I_{11} + \frac{1}{I_{11}} - 2\Big) + A_2\Big(I_{12} + \frac{1}{I_{12}} - 2\Big) + A_4\Big(I_{11} + I_{12} + \frac{1}{I_{23}} - 3\Big),$$

in which A_1, A_2 and A_4 are elastic parameters. The out-of-plane part of the elastic energy is chosen as

$$\rho_o\psi^{e_{op}} = H^+\rho_o\psi^{e_{top}} + (1 - H^+)\rho_o\psi^{e_{cop}} + \rho_o\psi^{e_{sop}}, \tag{2}$$

where the subscripts *top*, *cop* and *sop* refers to tension out-of-plane, compression out-of-plane and shear out-of-plane, respectively. The function H^+ is a switch function that takes the value 1 if $I_{13} - 1 > 0$ and zero otherwise, i.e. either $\psi^{e_{top}}$ or $\psi^{e_{cop}}$ is present in (2). The *top*, *cop* and *sop* part of the out-of-plane elastic free energy are given by

$$\rho_o\psi^{e_{top}} = A_3\Big(I_{13} + \frac{1}{I_{13}} - 2\Big), \quad \rho_o\psi^{e_{cop}} = A_6\Big(I_{13}^2 + \frac{1}{A_7}e^{-A_7((I_{13})^2-1)} - 2\Big),$$
$$\rho_o\psi^{e_{sop}} = A_5\Big(I_{11}I_{12}I_{13} - J^e\Big),$$

respectively. The total elastic part of the free energy (1) is for convenience summarized below

$$\begin{aligned}\rho_o\psi^e = {} & A_1\Big(I_{11} + \frac{1}{I_{11}} - 2\Big) + A_2\Big(I_{12} + \frac{1}{I_{12}} - 2\Big) + H^+A_3\Big(I_{13} + \frac{1}{I_{13}} - 2\Big) \\ & + A_4\Big(I_{11} + I_{12} + \frac{1}{I_{23}} - 3\Big) + A_5\Big(I_{11}I_{12}I_{13} - J^e\Big) \\ & + (1 - H^+)A_6\Big(I_{13}^2 + \frac{1}{A_7}e^{-A_7((I_{13})^2-1)} - 2\Big).\end{aligned} \tag{3}$$

It is mentioned that the free energy is chosen so that no initial Poisson's effect between the in-plane and out-of-plane is present, cf. Borgqvist (2016). The elastic parameters A_1, A_2, A_3, A_4, A_5 A_6 and A_7 are summarized in Table 2 below.

Table 2: Numerical values of elastic parameters.

Elastic parameter	**Value**
A_1 (MPa)	1721
A_2 (MPa)	404
A_3 (MPa)	21.1
A_4 (MPa)	1263
A_5 (MPa)	86
A_6 (MPa)	0.37
A_7 (-)	11.5

2.3.4 Plasticity

In the above section, the elastic part of the Helmholz' free energy was specified and a more precise format of the Kirchoff stress tensor was given. The plastic part of the free energy is now chosen as

$$\rho_o \psi^p = \sum_{\nu=\{1,2,3,6\}} a_{(\nu)} \Big(\frac{(b_{(\nu)}\kappa^{(\nu)}+1)}{b_{(\nu)}} \ln(b_{(\nu)}\kappa^{(\nu)}+1) - \kappa^{(\nu)} \Big) + \frac{1}{2} a_{(7)} \kappa^{(7)2}. \tag{4}$$

However, to begin with, the yield surface is explained. The yield surface was originally proposed by Xia et al. (2002) and then further developed by Borgqvist et al. (2014). The yield surface is chosen as

$$f(\boldsymbol{\tau}, \boldsymbol{n}_s^{(\beta)}, K^{(\beta)}) = \sum_{v=1}^{12} \chi^{(\nu)} \Omega_{(\nu)}^{2k} - 1, \tag{5}$$

where the parameter $\Omega_{(\nu)}$ is defined as

$$\Omega_{(\nu)} = \Big(\frac{\boldsymbol{\tau} : \boldsymbol{n}_s^{(\nu)}}{\tau^{(\nu)}} \Big).$$

The yield surface (5) consists of 12 subsurface, of which six belong to the in-plane stresses and the other six belong to the out-of-plane stresses. Note that in (5), $\boldsymbol{\tau}$ is as usual the Kirchoff stress tensor. Referring to Borgqvist et al. (2014), the normal tensors $\boldsymbol{n}_s^{(\nu)}$ are defined as

$$\boldsymbol{n}_s^{(\nu)} = \sum_{i=1}^{3} \sum_{j=1}^{3} N_{ij}^{(\nu)} \bar{\boldsymbol{v}}^{(i)} \otimes \bar{\boldsymbol{v}}^{(j)},$$

where $N_{ij}^{(\nu)}$ are constants associated with the respective yield subsurface ν and $\bar{\boldsymbol{v}}^{(i)}$ are the normed material direction vectors given by

$$\bar{\boldsymbol{v}}^{(1)} = \frac{\boldsymbol{v}^{(1)}}{|\boldsymbol{v}^{(1)}|}; \quad \bar{\boldsymbol{v}}^{(2)} = \frac{\boldsymbol{v}^{(2)}}{|\boldsymbol{v}^{(2)}|}; \quad \bar{\boldsymbol{v}}^{(3)} = \frac{\boldsymbol{n}^{(3)}}{|\boldsymbol{n}^{(3)}|}.$$

The stress $\tau^{(\nu)}$ represents the distance to corresponding current yield subsurface ν and is given by

$$\tau^{(\nu)} = K_o^{(\nu)} + K^{(\nu)},$$

where $K_o^{(\nu)}$ is the initial distance to the subsurface ν and $K^{(\nu)}$ is the hardening parameter defining the distance to the current yield subsurface, calculated as

$$K^{(\gamma)} = \rho_o \frac{\partial \psi^p}{\partial \kappa^{(\gamma)}}, \tag{6}$$

refer to appendix 7.1 for more details. Carrying out the derivative (6) with the potential part of the free energy according to (4), the hardening parameters are obtained

$$K^{(\nu)} = \begin{cases} a_{(\nu)} \ln(b_{(\nu)}\kappa^{(\nu)}+1) & \text{for } \nu = \{1,2,3,6\} \\ a_{(\nu)}\kappa^{(\nu)} & \text{for } \nu = 7 \\ 0 & \text{for } \nu = \{4,5,8,9,10,11,12\}, \end{cases}$$

which means that for the subsurfaces defining the in-plane stress state in tension and shear, as well as the subsurface associated with the ZD compression, i.e. for the subsurfaces $\nu \in \{1,2,3,6,7\}$, there exist a corresponding internal variable $\kappa^{(\nu)}$ to each hardening parameter, defining its evolution. Note that, as a consequence of the chosen potential function, for the remaining subsurfaces, ideal plasticity is assumed. The values of the initial yield $K_o^{(\nu)}$ and hardening parameters $a_{(\nu)}$ and $b_{(\nu)}$ are, for each subsurface, specified in Table 3 below.

Evaluating the yield function (5) further, k is a constant that changes the shape of the yield function, in particular the shape of its corners, and it is chosen to $k = 3$, which is in agreement with Borgqvist (2016). However, in Xia et al. (2002), the choice $k = 2$ was made. Finally, $\chi^{(\nu)}$ in (5) is a switch function, determining if the subsurface is active ore not, defined as

$$\chi^{(\nu)} = \begin{cases} 1 & \text{if } \Omega_{(\nu)} > 0 \\ 0 & \text{otherwise.} \end{cases}$$

Let us now consider the evolution laws. As usual, it is enforced that the yield function takes the value zero during plastic loading. Moreover, the plastic rate of deformation tensor, as well as the evolution of the internal variables, can be formulated in a general manner as

$$f = 0, \quad \boldsymbol{d}^p = \dot{\lambda}\frac{\partial f}{\partial \boldsymbol{\tau}}, \quad \dot{\kappa} = -\dot{\lambda}\frac{\partial f}{\partial K^{(\nu)}},$$

cf. Ristinmaa and Ottosen (2008). With the yield surface chosen according to (5), these relations can be specified further. Referring to Robertsson (2018), the following specific formats are obtained

$$\begin{aligned}
\boldsymbol{d}^p &= \dot{\lambda}\frac{\partial f}{\partial \boldsymbol{\tau}} = \dot{\lambda}\sum_{\nu=1}^{12}\Big(\frac{\partial f}{\partial \Omega_{(\nu)}}\frac{\partial \Omega_{(\nu)}}{\partial \boldsymbol{\tau}}\Big) = \dot{\lambda}\sum_{\nu=1}^{12}\Big(\big(\chi^{(\nu)}2k\Omega_{(\nu)}^{2k-1}\big)\big(\frac{\mathrm{sym}(\boldsymbol{n}_s^{(\nu)}}{\tau^{(\nu)}}\big)\Big) \\
&= \dot{\lambda}\sum_{\nu=1}^{12} H_{(\nu)}\mathrm{sym}(\boldsymbol{n}_s^{(\nu)}), \\
\dot{\kappa}^{(\nu)} &= -\dot{\lambda}\frac{\partial f}{\partial K^{(\nu)}} = -\dot{\lambda}\frac{\partial f}{\partial \Omega_{(\nu)}}\frac{\partial \Omega_{(\nu)}}{\partial K^{(\nu)}} = -\dot{\lambda}\Big(\chi^{(\nu)}2k\Omega_{(\nu)}^{2k-1}\Big)\Big((\boldsymbol{\tau}:\boldsymbol{n}_s^{(\nu)})\frac{\partial(\tau^{(\nu-1)})}{\partial \tau^{(\nu)}}\frac{\partial \tau^{(\nu)}}{K^{(\nu)}}\Big) \\
&= \dot{\lambda}\Big(\frac{2k\chi^{(\nu)}}{\tau^{(\nu)}}\Omega_{(\nu)}^{2k-1}\Big)\Big(\frac{\boldsymbol{\tau}:\boldsymbol{n}_s^{(\nu)}}{\tau^{(\nu)}}\Big) = \dot{\lambda}H_{(\nu)}\Omega_{(\nu)},
\end{aligned}$$

where

$$H_{(\nu)} = \frac{2k\chi^{(\nu)}}{\tau^{(\nu)}}\Omega_{(\nu)}^{2k-1}.$$

In order to establish the plastic velocity gradient $\boldsymbol{l}^p = \boldsymbol{d}^p + \boldsymbol{\omega}^p$, the plastic spin $\boldsymbol{\omega}^p$ must be specified. This is done in Borgqvist (2016), in which also a discussion regarding the implications of the plastic spin is provided. Important to note is that the plastic spin is chosen so that permanent deformations will not develop in the stacking direction during out-of-plane shearing, i.e. permanent deformations will only develop in the fibre directions.

Table 3: Numerical values of plastic parameters defining the subsurfaces of the yield function.

Subsurface, ν	**Stress state**	**Initial yield, K_o (MPa)**	**Hardening, $a_{(\nu)}$ (MPa)**	**Hardening, $b_{(\nu)}$ (-)**
1	MD-tension	17.687	14.3	299
2	CD-tension	10.460	6.7	211
3	MD-CD shear	8.623	11.2	83
4	MD-compression	22.062	-	-
5	CD-compression	16.704	-	-
6	CD-MD shear	8.623	11.2	83
7	ZD-compression	0.500	52.0	-
8	ZD-tension	0.439	-	-
9	MD-ZD shear	2.278	-	-
10	ZD-MD shear	2.278	-	-
11	CD-ZD shear	2.278	-	-
12	ZD-CD shear	2.278	-	-

2.4 Damage modeling in LS-Dyna using eGISSMO

In this section, the damage modeling in LS-Dyna is explained in a general sense. As stated already in the introduction, the damage is introduced in LS-Dyna as an add-on, on top of the existing continuum material model. Hence, no change of the material model, such as e.g. the description of the potential free energy, is made. The requirements that a damage model must fulfil are several. For example, it should be able to capture failure in several different modes and be easy to calibrate.

To start with, the **G**eneralized **I**ncremental **S**tress **S**tate dependent damage **Mo**del, GISSMO, is explained. GISSMO is a damage model that has been available in several versions of LS-Dyna and has the feature of handling isotropic damage. However, in LS-Dyna version R9, a new, *extended* version of this damage model, called eGISSMO, was introduced. This is a multi-parameter anisotropic damage model. The explanation of GISSMO and eGISSMO model is based on the manual provided by LS-Dyna, refer to Livermore Software Technology (2021). The GISSMO model is described in section 2.4.1 below, whereas eGISSMO is described in section 2.4.2.

2.4.1 GISSMO

The GISSMO model in LS-Dyna is based on continuum damage mechanics (CDM), a concept in which discontinuous growth of micro-voids and micro-cracks are considered as homogeneous and continuous and at a large level, cf. Erhart et al. (2017). This in accordance with the definition of continuum mechanics in general, which assumes that microscopic properties can be described at a macroscopic level. The essential concept in continuum damage mechanics is the concept of *effective stress*. The effective stress is the stress in the material when considering and assuming no strength of the defected area, A_{defect}, which consists of voids. The effective stress can be written as

$$\tilde{\boldsymbol{\sigma}} = \frac{F}{A - A_{defect}} = \frac{F}{A_{eff}}. \tag{7}$$

In the GISSMO model a variable which is called the *damage variable* is introduced. This variable defines the relation between the defected and total current area of the

cross section

$$D = \frac{A_{defect}}{A}. \tag{8}$$

By dividing (7) by the total current area A, and noting that the true stress can be written as $\boldsymbol{\sigma} = F/A$, the following expression is, after some rearrangement, found

$$\boldsymbol{\sigma} = (1 - \frac{A_{defect}}{A})\tilde{\boldsymbol{\sigma}} = (1 - D)\tilde{\boldsymbol{\sigma}}, \tag{9}$$

where $\boldsymbol{\sigma}$ is called the *damaged*, *true* or *nominal* stress, whereas $\tilde{\boldsymbol{\sigma}}$ is called the *undamaged* or *effective* stress. The evolution of damage represents the evolution of voids in the material. When there are no voids, the effective area equals the total cross-section area and the damage D is zero. However, when the entire cross section consists of voids, the effective area is zero and the damage D equals one. This leads to material failure. Note that when the damage grows, the nominal stress decreases. This means that a softening response can be introduced in the material. To evaluate (9) further, it is noted that the damage variable D is a scalar value. This means that all components of the effective stress tensor are scaled in a uniform manner. This is the reason for why GISSMO is called an *isotropic* damage model.

In general, two processes are of importance in damage modelling using GISSMO. The first process is the *instability* process, which defines the point at which the material reaches instability. Before material instability occurs, the material model, normally defined by the elasticity assumptions and the yield function with its corresponding plastic evolution laws, is sufficient for describing the behaviour of the material. However, when material instability occurs, the material softens and hence the unique solution is lost. Moreover, the model becomes mesh-dependent. The material instability is handled in GISSMO by the material instability variable F_D. When $F_D = 1$, material instability is reached. The second process of importance in GISSMO is the evolution of damage, which, as stated previously in (8), is handled by the damage variable D, defined as the ratio between the defected and total current cross-section area.

The concept of material instability and damage is depicted in Fig. 11 below. It is noted that in GISSMO both the material instability F_D and the damage D start to develop at the same point, namely at the start of plastic response. It is underlined that, although damage evolves, it is not coupled to the stresses until material instability is reached. i.e. (9) does not apply until $F_D = 1$.

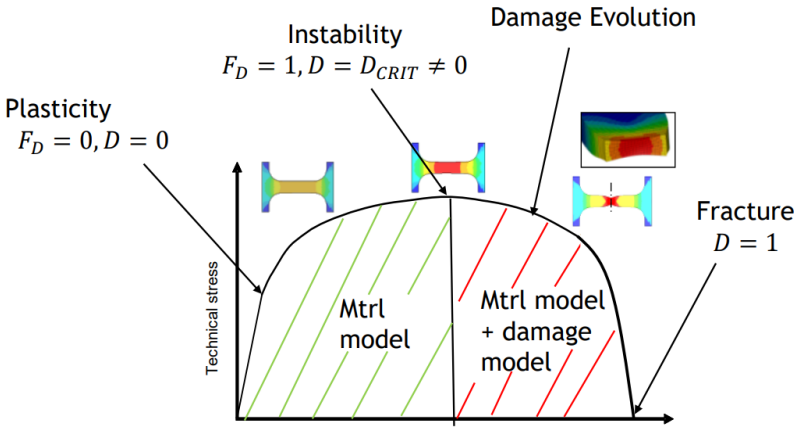

Figure 11: The concept of the evolution of material instability and damage. Source: Dynamore.

However, when material instability is reached, $F_D = 1$, the damage variable D, which at this point equals $D = D_{CRIT}$, is coupled to the stress, i.e. (9) applies. The damage variable is then allowed to evolve further, and when $D = 1$ in a user defined number of integration points of the element, the element is deleted. Material instability and damage evolves according to evolution laws which are of the same principal format

$$\Delta F = nF^{(1-\frac{1}{n})}\frac{\Delta HIS}{\varepsilon_i(\eta^*)}, \tag{10a}$$

$$\Delta D = nD^{(1-\frac{1}{n})}\frac{\Delta HIS}{\varepsilon_f(\eta^*)}, \tag{10b}$$

where ΔHIS is the driving history variable, which can be chosen either directly from the strain tensor or as any user defined function of some arbitrary history variable such as a strain measure in a certain direction. Moreover, it is observed that the material instability and damage evolution laws both have a non-linear term n, which is referred to as the *damage exponent*. The damage exponent can be used to calibrate the response. The functions $\varepsilon_i(\eta^*)$ in (10a) and $\varepsilon_f(\eta^*)$ in (10b) are the material instability function and failure function, respectively. The subscript i denotes instability whereas the subscript f denotes failure. The two functions determines the amount of instability and damage that evolves due to the increment in the chosen history variable, ΔHIS. In Fig. 12 below, the failure function is plotted in blue, whereas the history variable is plotted in red. It is noted that the failure function is a function of the stress triaxiality η, which is defined as the *hydrostatic stress* divided by the *effective von Mises stress*

$$\eta = \frac{\sigma_m}{\sigma_{eq}} = \frac{\frac{1}{3}(\sigma_{11} + \sigma_{22} + \sigma_{33})}{\sqrt{3J_2}},$$

where J_2 is the second invariant of the deviatoric stress tensor. Stress triaxiality is a common measure in fracture mechanics and indicates whether the stress is primarily hydrostatic or deviatoric. It is noted in Fig. 12 that for a given increment in the history variable, ΔHIS, the larger the failure function is at the current triaxiality, the lower the increment in the damage variable, ΔD, becomes. As has already been

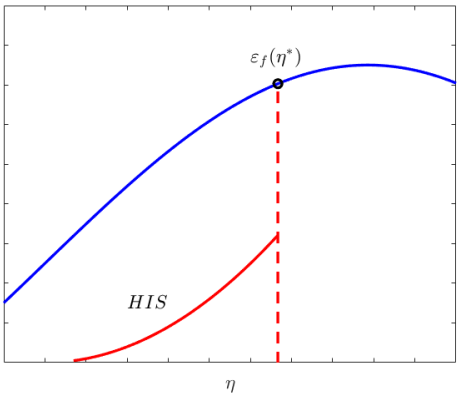

Figure 12: Illustration of the failure function ε_f (blue) and driving history variable HIS (red) at different stress triaxialities. The same concept applies for the material instability.

mentioned, when material instability is reached, the damage is coupled to the stress. It is desired that the true and effective stress are equal at the start of the coupling, i.e. $\tilde{\boldsymbol{\sigma}} = \boldsymbol{\sigma}$ when $D = D_{CRIT}$. Thus, (9) is slightly rewritten as

$$\boldsymbol{\sigma} = \Big(1 - \Big(\frac{D - D_{CRIT}}{1 - D_{CRIT}}\Big)^{\text{FADEXP}}\Big)\tilde{\boldsymbol{\sigma}},$$

in which a fading exponent constant FADEXP is introduced by which the coupling can be made non-linear. Moreover, FADEXP can be used to calibrate the response of the material. It is noted that if the fraction in the second term is smaller than one, then a higher FADEXP increases the damaged stress. Now, that the GISSMO model has been explained, the extended version of this model, eGISSMO, is in the following section presented.

2.4.2 eGISSMO

The extended version of GISSMO is called eGISSMO. In this, up to three different GISSMO models can be combined. In the literature, two types of *anisotropic damage* are common, cf. Erhart et al. (2017). The first type is called *Load Induced Anisotropy in Damage* (LIAD), and refers simply to the loading direction, e.g. if the material is loaded in the first principal material direction then the damage should also evolve the most in this direction. The second type of anisotropic damage refers to the material itself and is called *Material Induced Anisotropy in Damage* (MIAD). It is once again underlined that the paperboard material considered in this work inherits strong material anisotropic behaviour due to its manufacturing process. The extended version of GISSMO, eGISSMO, is able to describe both load induced (LIAD) and material induced (MIAD) anisotropy. To model anisotropic damage, the nominal-effective stress relation is described by a fourth-order tensor

$$\boldsymbol{\sigma} = \boldsymbol{M}^{-1} : \tilde{\boldsymbol{\sigma}}, \tag{11}$$

where $\boldsymbol{M}$ is called the *damage-effect tensor*. As Voigt notation is used, and the description is three-dimensional, this tensor takes the format of a 6x6 matrix, which is denoted $\boldsymbol{D}$ and called the *damage matrix*. Hence, using Voigt notation, (11) takes the format

$$\begin{bmatrix} \sigma_{11} \\ \sigma_{22} \\ \sigma_{33} \\ \sigma_{12} \\ \sigma_{23} \\ \sigma_{13} \end{bmatrix} = \begin{bmatrix} D_{11} & D_{12} & D_{13} & & & \\ D_{21} & D_{22} & D_{23} & & & \\ D_{31} & D_{32} & D_{33} & & & \\ & & & D_{44} & & \\ & & & & D_{55} & \\ & & & & & D_{66} \end{bmatrix} \begin{bmatrix} \tilde{\sigma}_{11} \\ \tilde{\sigma}_{22} \\ \tilde{\sigma}_{33} \\ \tilde{\sigma}_{12} \\ \tilde{\sigma}_{23} \\ \tilde{\sigma}_{13} \end{bmatrix},$$

which in shorter notation reads

$$\boldsymbol{\sigma} = \boldsymbol{D}\tilde{\boldsymbol{\sigma}}. \tag{12}$$

In the above, each component D_{ij} of the damage matrix $\boldsymbol{D}$ can in eGISSMO be defined as a function of up to three damage variables

$$D_{ij} = f(d_1, d_2, d_3). \tag{13}$$

The evolution of the material instability and damage is defined for each damage and instability variable separately as

$$\Delta f_j = n_j f_j^{(1-\frac{1}{n_j})} \frac{\Delta HIS_j}{\varepsilon_{i,j}(\eta^*)}, \tag{14a}$$

$$\Delta d_j = n_j d_j^{(1-\frac{1}{n_j})} \frac{\Delta HIS_j}{\varepsilon_{f,j}(\eta^*)}, \tag{14b}$$

where the subscript j is either 1,2 or 3. It is mentioned that the damage exponent n is sometimes denoted DMGEXP. It is also noted that any arbitrary history variable ΔHIS can be chosen to drive the evolution of the damage variable. It is, in particular, emphasized that each damage and instability variable can be driven by a unique history variable. Finally, it is mentioned that the coupling between the undamaged and damaged stresses in eGISSMO is in agreement with the GISSMO model. However, since up to three different damage variables are present, each damage variable is separately considered. Thus, each damage variable is when coupled to the stress replaced by

$$d_j \to \Big(\frac{d_j - d_{CRIT_j}}{1 - d_{CRIT_j}}\Big)^{\mathrm{FADEXP}_j}, \tag{15}$$

cf. Erhart et al. (2017).

3 Simulation without damage

The simulation of the creasing and folding operations without damage is presented in this section. The creasing operation is described in section 3.1, whereas the folding operation is described in section 3.2.

3.1 Line creasing operation

The simulation setup of the line creasing setup is explained in section 3.1.1. The corresponding results are presented in section 3.1.2.

3.1.1 Method

In this section, the simulation setup of the line creasing method is explained. To start with, it is noted that a fixed geometry of the paperboard and the dies is adopted. The geometrical quantities, depicted in Figs. 5 and 6 above, are now described. The paperboard specimen has a length of 110 mm, a width of 38 mm and a thickness of 0.39 mm. The width of the male die is 0.9 mm and the width of the female die is 1.7 mm. The prescribed displacement u_w is applied at the ends of the paperboard ply so that an initial force of 58 N is obtained. Since the paperboard is 38 mm wide, this corresponds to a distributed force of 1.5 kN/m along the width. The creasing depth is defined as the distance that the male die penetrates the female die. Hence, when the male and female die are aligned, the creasing depth is zero. A creasing depth of 0.18 mm has been adopted in this work. The radius of the corners of the male and female die is specified to 0.1 mm.

In the simulations, a reduced geometry of the paperboard ply, then what is the case for the standard test setup is adopted. To be more specific, the width of the paperboard is in the simulation model put to 0.1 mm instead of 38 mm. This is done to reduce the computational cost. It is emphasized that reducing the width of the geometry is possible as long as everything is scaled correctly. By adopting the width 0.1 mm, the correct scaled pretension displacement is calculated to 0.039 mm, refer to Appendix 7.2. The creasing depth, pretension displacement and the geometrical quantities used in the simulation setup are all summarized in Table 4.

The male- and female dies are in LS-Dyna modelled as rigid parts. The friction coefficient between the tools and the paperboard is tested for both 0.30 and 0.40, where the latter is in accordance with Borgqvist (2016). Referring to Borgqvist (2016), it is emphasized that the friction coefficient between the tools and paperboard has a large influence on the simulation results. The prescribed web-tension u_w is applied at both ends of the paperboard. Displacements are prescribed to zero in the CD-direction at both sides along the length of the paperboard. This is due to that the actual specimen is 38 mm wide and therefore prevents movement in the CD-direction of the central 0.1 mm wide part of the specimen considered in the simulations. At the ends of the ply, the displacement in both the CD- and ZD-direction is prescribed to zero.

A fixed mesh of the paperboard ply using 25 elements through the thickness and one element through the width is adopted. Along the length of the ply, three different mesh sizes are used, where the mesh size is finer in regions subjected to higher stresses. The element length is taken as 1.06 mm, 0.28 mm and 0.07 mm in the outer, outer-central and central region of the paperboard, respectively. The simulation model of

the line creasing operation, including the paperboard ply and the male- and the female die, is depicted in Fig. 13.

When the simulations are finished, a central part of the paperboard, with a length of 25 mm, is exported as an output file with the format `dynain`. The output file contains the final stress situation in the creased specimen with all history variables stored. The reason for cutting the creased specimen into a smaller part is to save computational cost. Before entering the folding simulation, the part is allowed to release. To do this, the model is imported to a separate simulation called the releasing simulation. In this simulation, the model is only fixed in two nodes such that rigid body motion is avoided.

Table 4: Geometrical quantities and prescribed crease depth of the line creasing simulation.

Quantity	**Value (mm)**
Paperboard length	110
Paperboard width	0.1
Paperboard thickness	0.39
Male die width	0.9
Female die width	1.7
Radius	0.1
Prescribed pretension	0.036
Creasing depth	0.18

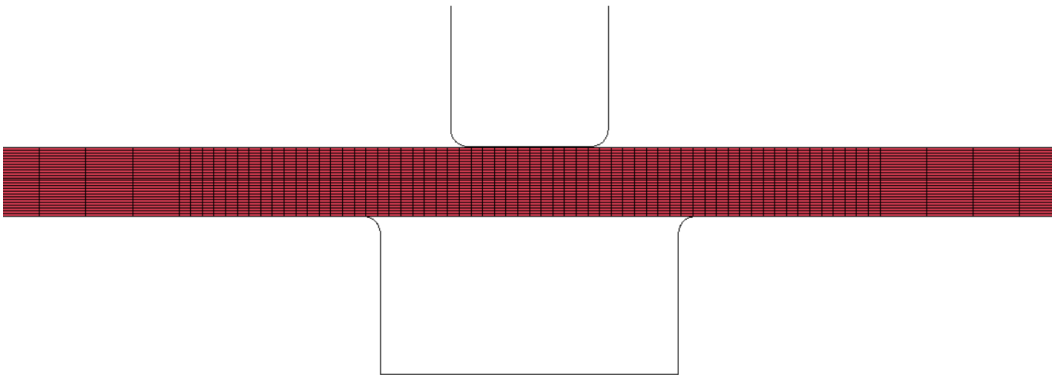

Figure 13: Simulation model of the line creasing operation. The model has 25 elements through the thickness and one element through the width. Note that different mesh sizes have been adopted along the length of the paperboard ply. Note also the geometry and location of the male and female die, above and below the paperboard ply, respectively.

3.1.2 Results

In this section, the results of the line creasing simulation are presented. In Fig. 14a, the male die force is plotted against the male displacement, whereas in Fig. 14b, the in-plane force is plotted against the male displacement. Observe in the figures that the simulation with friction coefficient FS=0.4 between the tools is in better agreement with the measured data. Thus, FS=0.4 is used in the following simulations. Observing Fig. 14a, it is noted that the simulation results of the reaction force of the male die vs. the male die displacement well aligns with the experimental data. However, the male force is during unloading a bit too overestimated. Observing instead Fig. 14b, the simulations and experimental data is only in agreement until a displacement of about -0.2 mm. After this, the simulations predict a too high in-plane force. The force is overestimated also during unloading.

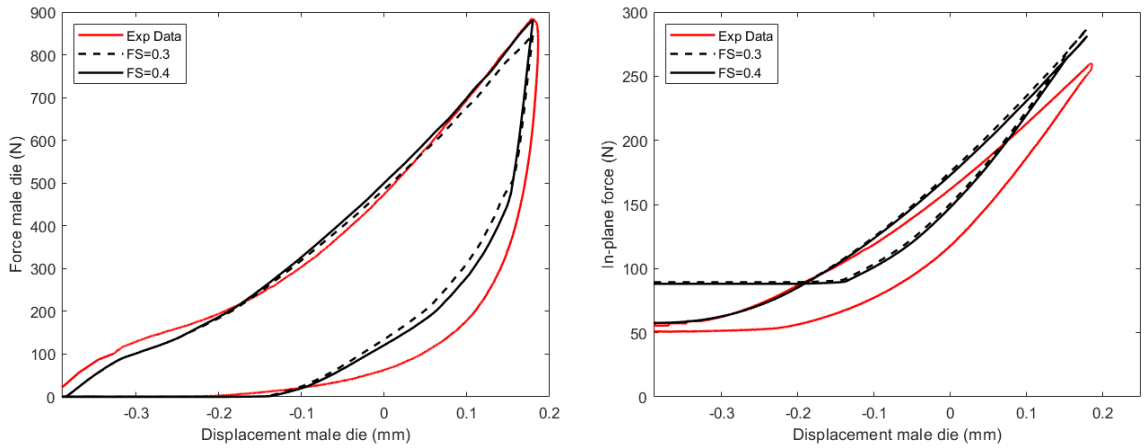

(a) Plot of reaction force of male die vs male die displacement during creasing for experimental data (red) and simulation (black).

(b) Plot of in-plane force paperboard vs male die displacement during creasing for experimental data (red) and simulation (black).

Figure 14: Force in the male die and paperboard during line creasing operation. Observe that different friction coefficients have been used.

The deformed shape of the paperboard after creasing is shown in Figs. 15 and 16. In Fig. 15, the out-of-plane plastic shear strain κ_{sop} is visualised, and it is evident that this strain is significant. It is noted that the strain is localised in the area where the corners of the male die penetrate the paperboard ply. In Fig. 16, the plastic strain in the ZD-direction, $\kappa^{(8)}$, is visualised. Also this strain, which develops during the unloading of the male die, is large. However, the magnitude of the shear strain is about twice as large as the tension strain. The tension strain is localised in the central, lower half of the paperboard ply.

As significant strain develops in the out-of-plane shear and tension directions, it can be presumed that it is a good idea to state that damage is induced in the paperboard in one or both of these directions. This is investigated further in section 4, in which the plastic shear and tension in the out-of-plane direction are separately considered to drive the evolution of damage in the material.

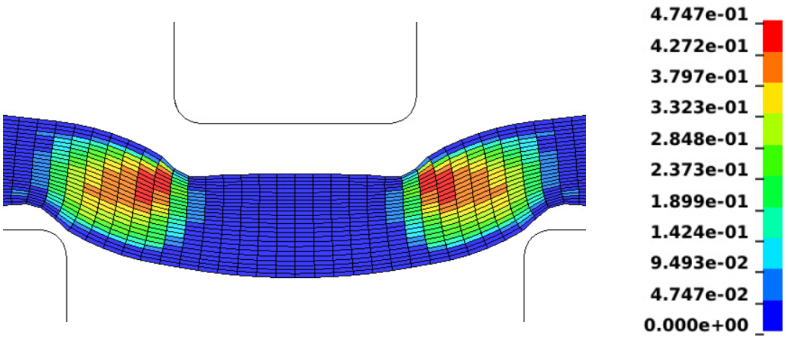

Figure 15: Plastic out-of-plane shear strain κ_{sop} at the end of the line creasing operation. The plastic strain is localised in the area where the corners of the male die penetrates the paperboard ply.

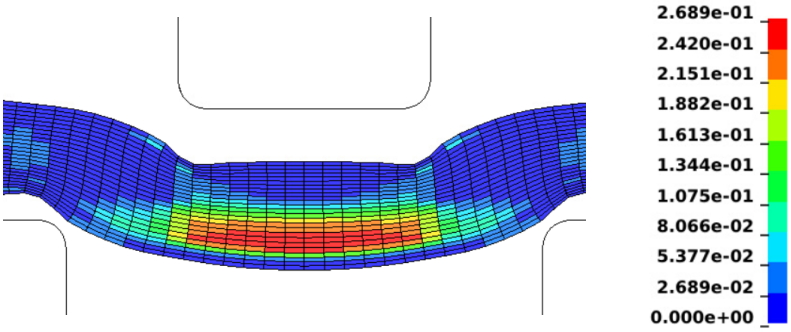

Figure 16: Plastic out-of-plane tension strain at the end of the line creasing operation. The plastic strain is localised in the lower half of the paperboard ply and develops during unloading of the male die.

3.2 Line folding operation

The simulation setup of the line folding setup is explained in section 3.2.1. The corresponding results are presented in section 3.2.2.

3.2.1 Method

In this section, the simulation setup of the line folding operation is explained. To start with, it is noted that a fixed geometry of the paperboard ply, the load cell and the two clamps is adopted. The geometrical quantities are depicted in Figs. 7 and 8 above. The paperboard is, as stated in section 3.1.1 above, cut after the creasing operation, and thus has a length of 25 mm. The width and thickness are still 0.1 and 0.39 mm, respectively. The width of the clamps is 10 mm and the width of the load cell is 0.8 mm. The clamping pressure is chosen as 0.2 MPa, which is in correspondence with Borgqvist (2016). The distance l_o between the end of the clamps and the load cell is chosen to 10 mm. The distance between the ends of the clamps and the centre of the crease line is chosen as 2 mm. The geometrical quantities of all parts in the folding operation are summarized in Table 5. The simulation model of the line folding operation, including the paperboard ply and the two clamps, is depicted in Fig. 17.

The two clamps are modelled as rigid parts. The friction coefficient between the tools and the paperboard is set to 0.40, as this is the coefficient leading to the best prediction of the creasing operation, refer to section 3.1.2. Displacements are, similar to the creasing setup, prescribed to zero in the CD-direction at both sides along both lengths of the paperboard. The paperboard is rotated 90 degrees. The rotational centre of each clamp is specified as the left end of the clamp itself, refer to Fig. 17. The folding operation is undertaken both for creased and uncreased paperboard.

Table 5: Geometrical quantities of the line folding simulation.

Quantity	**Value (mm)**
Paperboard free length	25
Clamp lengths	10
Load cell length	0.8
Distance between clamps and load cell	10
Distance between clamps and centre of crease line	2

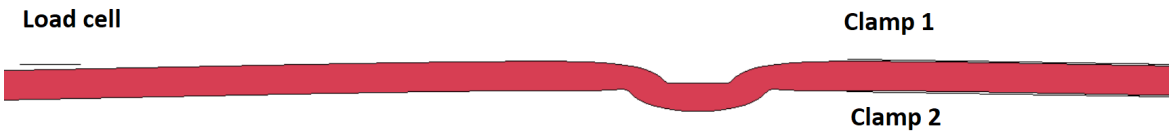

Figure 17: Simulation model of folding of creased paperboard. The paperboard model is imported from the line creasing simulation. Note the load cell to the left and the two clamps, which will press and rotate the paperboard, to the right.

3.2.2 Results

In this section, the results of the line folding simulation for creased and uncreased paperboard are presented. The focus is on presenting the results of the folding of creased paperboard, as the simulation prediction in this case is not in good agreement with the measured data.

Folding of creased paperboard
For folding of creased paperboard, the reaction force is predicted correctly at the initial part of the operation, refer to Fig. 18. However, for the measured data, the stiffness decreases at about 10 degrees of bending. A stiffness change is also observed in the simulation results, but this change is much smaller. Thus, the reaction force is overestimated in the simulation. Moreover, it is evident from Fig. 18 that whereas the measured data shows that the reaction force is rather constant, this is not the case for the simulated response. Instead, the force increases continuously. The folding of creased paperboard is studied further below.

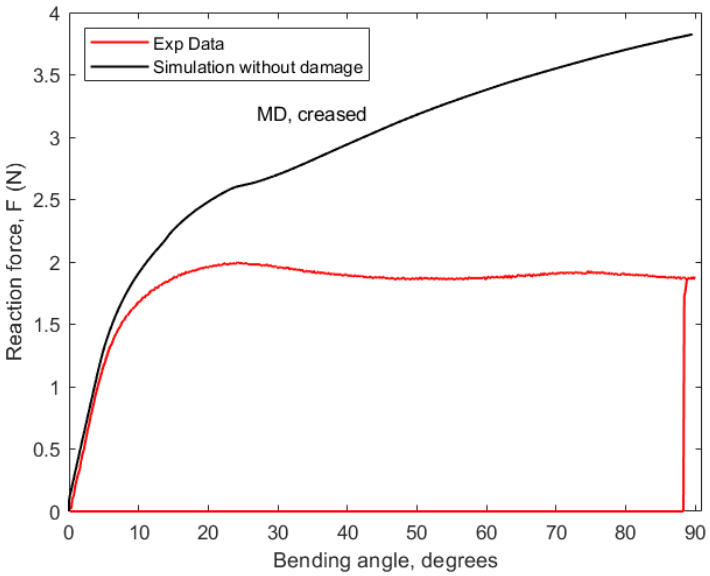

Figure 18: Plot of reaction force of load cell vs the bending angle during folding in the MD-direction for creased paperboard. The red curve indicates experimental data and the black curve indicates simulation results for which no damage is included.

The out-of-plane plastic shear strains κ_{sop} are visualized in Table 6 at bending angles of 0, 10, 20, 30, 40, 50 and 60 degrees. It is noted that the shear strain develops rather modestly from 0 to 10 degrees. The development is then only slightly more accentuated from 10 to 20 degrees. However, as the folding continuous, large strains develop.

Table 6: Out-of-plane shear strain κ_{sop} at bending angles of 0, 10, 20, 30, 40, 50 and 60 degrees. The same scale is used in all subfigures. Note that the development of the plastic strain κ_{sop} is small at the initial part of the folding operation.

Bending angle:		Bending angle:	
0°	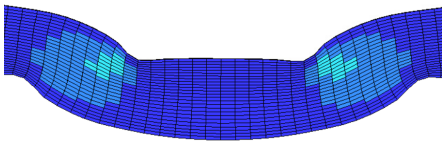	**40°**	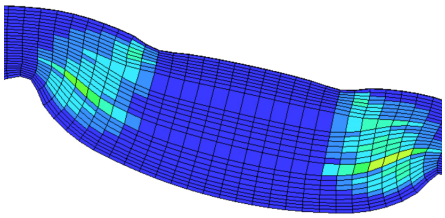
10°	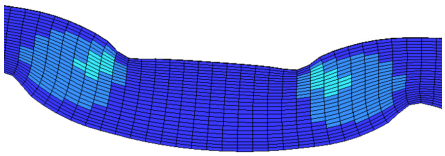	**50°**	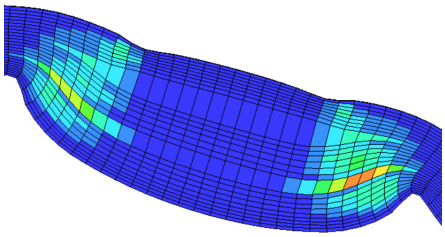
20°	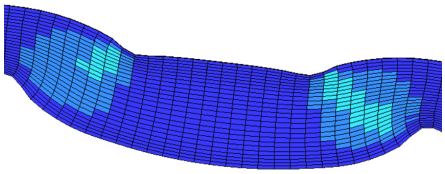	**60°**	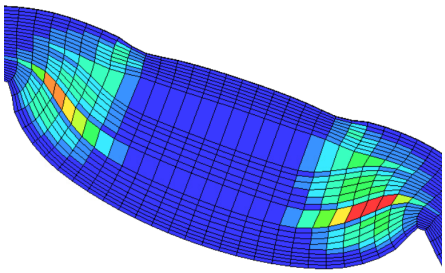
30°	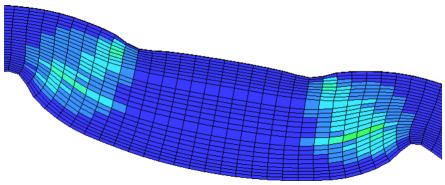		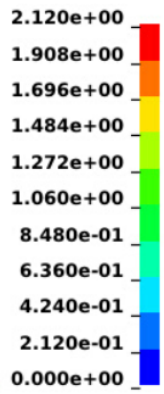

To proceed, comparing the simulated response at 60 degrees of bending with the actual observed deformation, refer to Fig. 19, it is noted that micro-cracks observed in the experiments near the clamps are not predicted by the simulation. This is natural since the model without damage does not allow for any element erosion to take place. Furthermore, the simulation does not exhibit the delamination observed in the experimental testing.

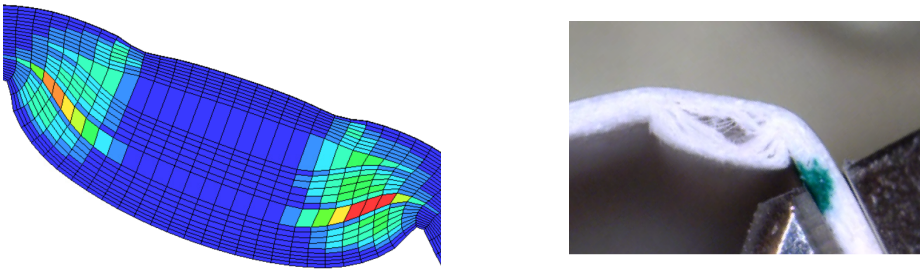

Figure 19: Comparison of the simulated response with the actual deformation at 60 degrees of bending. The formation of cracks near the clamps as well as the asymmetry of the cracks is not predicted by the simulation. Neither does the simulation predict the well defined delamination in the middle of the creased zone.

Comparing finally the out-of-plane plastic tension strain $\kappa^{(8)}$ for bending angles of 0, 10, 20, 30, 40, 50 and 60 degrees, refer to Table. 7, it is noted that the development of $\kappa^{(8)}$, just as κ_{sop}, is very modest from 0 to 10 degrees. However, the strain develops slightly more from 10 to 20 degrees. For large bending angles, substantial out-of-plane tension is observed.

Table 7: Out-of-plane tension strain $\kappa^{(8)}$ at bending angles of 0, 10, 20, 30, 40, 50 and 60 degrees. Note that the same scale is used in all three subfigures. Note that the development $\kappa^{(8)}$ is small at the initial part of the folding, especially from 0 to 10 degrees.

Bending angle:		Bending angle:	
0°	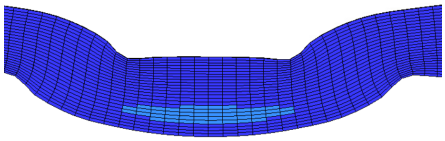	**40°**	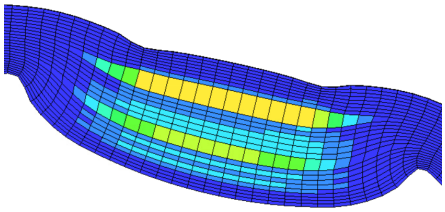
10°	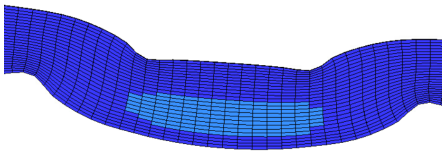	**50°**	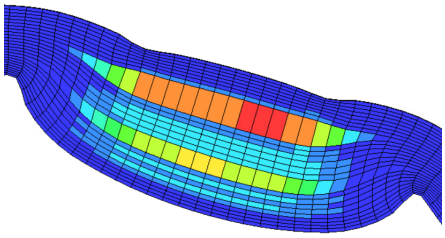
20°	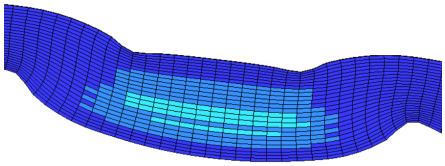	**60°**	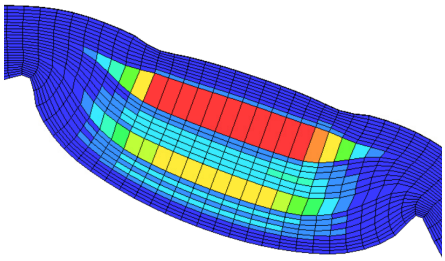
30°	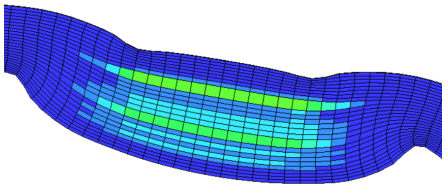		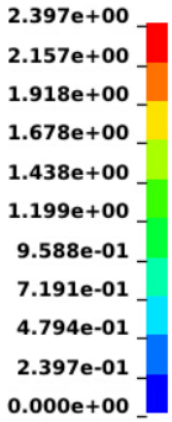

Folding of uncreased paperboard and RCS

Finally, the folding response of uncreased paperboard is provided, refer to Fig. 20. It is noted that the simulation predicts the reaction force lower than the measured data. However, the difference between the simulation and the measured data is rather small. The RCS value is calculated to

$$\text{RCS} = \frac{P^{max}_{b,creased,0<\theta<30}}{P^{max}_{b,uncreased,0<\theta<30}} = \frac{2.7}{4.4} = 0.61,$$

which deviates from the measured data, for which RCS = 0.39, with a relative difference of $(0.61 - 0.39)/0.61 = 36\%$.

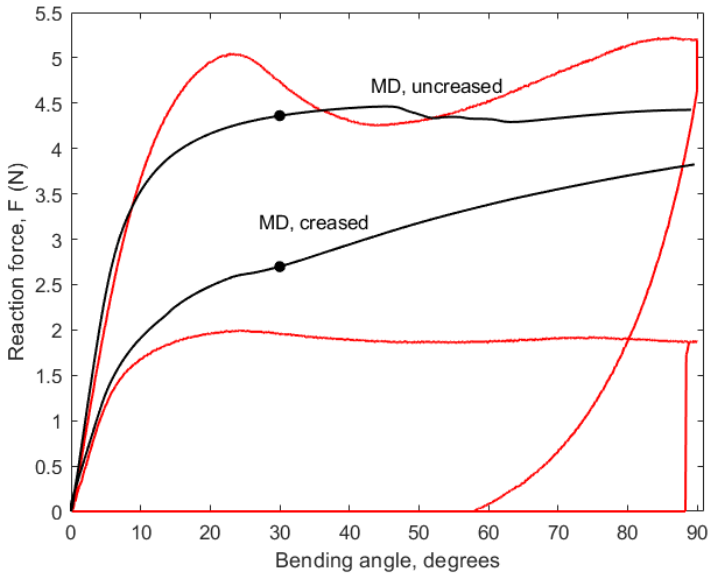

Figure 20: Plot of reaction force of load cell vs the bending angle during folding in the MD-direction for both creased and uncreased paperboard. The red curve represents experimental data and the black curve represents simulation results for the simulation without damage.

4 Simulation with damage

Referring to the obtained results of the folding operation without damage, the predicted response for the folding of the creased paperboard is overestimated. Therefore, damage modeling is introduced obtain a better prediction of the *folding of MD creased paperboard*. Damage is introduced by using eGISSMO, as stated in section 2.4. Damage is included both in the creasing and folding operation. Moreover, to obtain a physical sound description, the same damage model is used both during creasing and folding. This means that the parameters in (14a) and (14b) are specified before the start of the creasing operation and then held constant during both the creasing and subsequent folding operation. The model setup of creasing and folding is, apart from the introduction of damage, the same as described for the simulation without damage.

As evident in (14a) and (14b), many parameters can be varied in the eGISSMO damage model. However, to be able to identify what quantities affect the material response, the damage model is simplified. To start with, the damage exponent is chosen as $n = 1$ for the evolution of both instability and failure. Moreover, the instability and failure functions ε_i and ε_f are chosen as constant value functions. With these choices, the evolution laws (14a) and (14b) take the format

$$\Delta f_j = \frac{\Delta HIS_j}{\varepsilon_{i,j}}, \tag{16a}$$

$$\Delta d_j = \frac{\Delta HIS_j}{\varepsilon_{f,j}}. \tag{16b}$$

Considering the stress coupling equation, (15), the fading exponent is chosen as FADEXP=1. Thus, the stress coupling for each damage variable takes the format

$$d_j \rightarrow \frac{d_j - d_{CRIT_j}}{1 - d_{CRIT_j}}. \tag{17}$$

With the evolution laws simplified to the formats (16a) and (16b), and the stress coupling to (17), only the constant values of the instability and failure function, ε_i and ε_f, and the driving history variables ΔHIS_j are left to be specified. In this work, only one driving history variable is considered. As has previously been discussed, out-of-plane shear and tension are two potentially important deformation mechanisms when considering folding of MD creased paperboard. Actually, it is observed from the simulation without damage that these strains develop significantly. Hence, two damage models are investigated in this work. In the first investigation, the out-of-plane plastic shear strain

$$\kappa_{sop} = \kappa^{(9)} + \kappa^{(10)},$$

is chosen as the driving history variable. The reason for adding the out-of-plane plastic shear quantities is that these quantities are defined in the positive and negative MD-ZD direction, refer to Table 3. Hence, to obtain the full out-of-plane shear situation, i.e. the shear strains on both sides of the male die, these quantities must be added. In the second investigation, the plastic out-of-plane tension strain, $\kappa^{(8)}$, is chosen as the driving history variable. When the history variable is chosen, what remains is to choose the constant values of the instability and failure function. These functions are chosen iteratively. Hence, a calibration procedure is needed to investigate whether it is possible to predict the folding response of MD creased paperboard.

The calibration using κ_{sop} as the history variable is presented in section 4.1, whereas the calibration using $\kappa^{(8)}$ is presented in section 4.2. The simulation setup of the creasing and folding is, apart from the incorporation of damage, the same as for the simulation without damage.

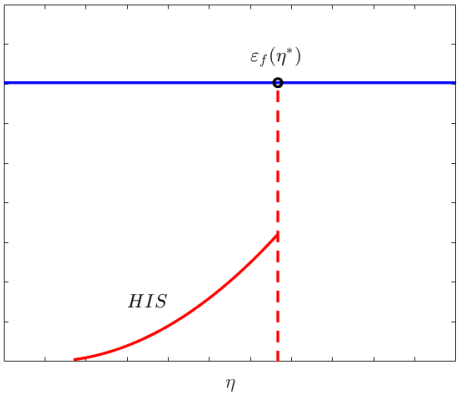

Figure 21: The failure function is chosen as a constant value function not depending on the triaxiality. The instability function is also chosen as a constant function.

4.1 Calibrating folding of creased paperboard by using out-of-plane plastic shear strain as driving history variable

In this section, the results of the creasing and folding operation simulated with damage, using the out-of-plane shear strain as the driving history variable, is presented. The simulation setup is presented in section 4.1.1, and the corresponding results are presented in section 4.1.2.

4.1.1 Method

As stated above, in this first approach to calibrate the folding response of creased paperboard, the driving history variable is chosen as

$$\Delta HIS = \kappa_{sop}.$$

With the history variable chosen, what remains is to choose the values of the instability and damage function ε_i and ε_f, refer to (16a) and (16b), as well as the damage matrix present in the stress coupling, refer to (12).

To start with, a calibration setup is made in which a total number of 16 simulations are carried out with different instability and failure functions, ε_i and ε_f. The functions are chosen to enable easy comparison to get an understanding of the effects of damage and instability. The stress coupling is specified to be isotropic. Referring to (13), this means that the diagonal components of the damage matrix is chosen as $D_{11} = D_{22} = D_{33} = D_{44} = D_{55} = D_{66} = 1 - d_1$, and that all the non-diagonal elements are set to zero. Thus, the relation between the damaged and undamaged stress takes the format

$$\begin{bmatrix} \sigma_{11} \\ \sigma_{22} \\ \sigma_{33} \\ \sigma_{12} \\ \sigma_{23} \\ \sigma_{13} \end{bmatrix} = (1 - d_1) \begin{bmatrix} 1 & & & & & \\ & 1 & & & & \\ & & 1 & & & \\ & & & 1 & & \\ & & & & 1 & \\ & & & & & 1 \end{bmatrix} \begin{bmatrix} \tilde{\sigma}_{11} \\ \tilde{\sigma}_{22} \\ \tilde{\sigma}_{33} \\ \tilde{\sigma}_{12} \\ \tilde{\sigma}_{23} \\ \tilde{\sigma}_{13} \end{bmatrix},$$

where it is evident that only one damage variable d_1 is present. The calibration, which is referred to as *calibration setup 1*, is specified in Table 8 below.

In the evaluation of the results of calibration setup 1, it was stated that the response is not sufficiently close to the measured data, and therefore needs to be calibrated further. Hence, a new, more precise, calibration is made in which the failure function is held between $1.2 \leq \varepsilon_f \leq 1.4$ and the instability function below $\varepsilon_i \leq 0.2$. The calibration, which is referred to as *calibration setup 2*, is specified in Table 8. The damage matrix is, as in calibration setup 1, chosen as isotropic.

However, also for calibration setup 2, a response that could be further calibrated is obtained. It is stated when evaluating the results that the failure function should be chosen as $\varepsilon_f = 1.40$, and the instability function varied between $0.10 < \varepsilon_i < 0.15$. Calibration setup 3 is specified in Table 8 by red triangles. The damage matrix is, as for calibration setup 1 and 2, chosen as isotropic.

Table 8: The instability and failure function used in the different calibration setups. The black circles, blue squares, and red triangles refer to calibration setup 1, 2, and 3, respectively.

ε_f \ ε_i	**0.05**	**0.10**	**0.11**	**0.12**	**0.13**	**0.14**	**0.15**	**0.20**	**0.30**	**0.40**	**0.50**
1.00								●	●	●	●
1.20								●	●	●	●
1.25	■	■					■	■			
1.30	■	■					■	■			
1.35	■	■					■	■			
1.40	■	■	▲	▲	▲	▲	■	●	●	●	●
1.60								●	●	●	●

Finally, to obtain more insight in the folding operation, different formats of the damage matrix are investigated. The investigation is made for the simulation in best agreement with the measured data. For each simulation, one diagonal element in the otherwise isotropic damage matrix is set to unity, refer to Table 9. To illustrate the approach, it is for example noted that the damage matrix for the third simulation takes the format

$$\begin{bmatrix} \sigma_{11} \\ \sigma_{22} \\ \sigma_{33} \\ \sigma_{12} \\ \sigma_{23} \\ \sigma_{13} \end{bmatrix} = \begin{bmatrix} (1-d_1) & & & & & \\ & (1-d_1) & & & & \\ & & 1 & & & \\ & & & (1-d_1) & & \\ & & & & (1-d_1) & \\ & & & & & (1-d_1) \end{bmatrix} \begin{bmatrix} \tilde{\sigma}_{11} \\ \tilde{\sigma}_{22} \\ \tilde{\sigma}_{33} \\ \tilde{\sigma}_{12} \\ \tilde{\sigma}_{23} \\ \tilde{\sigma}_{13} \end{bmatrix},$$

i.e. no damage is in this case coupled to the stress in the out-of-plane direction, σ_{33}.

Table 9: Simulation setup for investigating the response of different types of damage matrices. Note that the same instability and failure functions are used in all simulations.

Simulation nr.	**Index in damage matrix set to unity**	ε_i	ε_f
1	(1,1)	0.14	1.40
2	(2,2)	0.14	1.40
3	(3,3)	0.14	1.40
4	(4,4)	0.14	1.40
5	(5,5)	0.14	1.40
6	(6,6)	0.14	1.40

4.1.2 Results

The results from the simulation with damage with the out-of-plane shear strain as the driving history variable is presented here. To start with, only the folding response of creased paperboard is presented. First, the folding results from calibration setup 1, 2 and 3 are presented. It is concluded that the best fit is obtained in calibration setup 3. For the best calibration, the creasing operation is evaluated as well as the strains and deformed shape during folding of creased paperboard. Moreover, the folding of uncreased paperboard, using the damage leading to the best prediction of folding of creased paperboard, is presented.

Calibration setup 1

The simulation results of the folding operation from the damage assumptions specified in calibration setup 1, refer to Table 8, are presented in this section. The simulations have been structured to illustrate the effect of varying the failure and instability functions in the eGISSMO damage model during folding. The simulation results are presented in Fig. 22 below. In each subfigure, simulations with different instability values but the same constant damage value is plotted.

Comparing the folding results presented in the different subfigures in Fig. 22 in general, it is noted that increasing the damage, i.e. using a lower failure function ε_f, leads to a lower predicted reaction force. It is also evident that a lower failure function suggests a more varied, unstable and fluctuating response, especially for large bending angles. Considering instead the instability, i.e. comparing the different plots in each subfigure, it is noted that a higher instability evolution, i.e. a lower instability function ε_i, leads to a lower predicted reaction force.

Considering Fig. 22(a), i.e the simulations with failure function $\varepsilon_f = 1.0$, it is noted that the simulations in which the instability function are $\varepsilon_i = 0.2$ and $\varepsilon_i = 0.3$ best fits the measured data at the initial point. However, for larger bending angles these simulations predict the reaction force too low. In general, the simulation results are unstable using this failure function. Increasing the failure function to $\varepsilon_f = 1.2$, refer to Fig. 22(b), a more constant response is obtained. However, the response is still irregular and unstable in comparison with the almost constant measured data. It is also noted that the initial response is high for all simulation except $\varepsilon_i = 0.2$ in this case. Increasing the failure function further to $\varepsilon_f = 1.4$, refer to Fig. 22(c), a sufficient constant response is obtained. However, in this case not only the initial but the overall reaction force is overestimated. Finally, it is noted that using $\varepsilon_f = 1.6$, refer to Fig. 22(d), the overall prediction of the reaction force is even more overestimated.

To summarize the results, it is concluded that the failure function ε_f cannot be too low since, in that case, the response becomes too low and unstable. However, the failure function can neither be too high, since this leads to a prediction that overestimates the reaction force. By evaluating the simulation results in Fig. 22, it seems reasonable to make a new series of simulations in which the constant failure function is held between $1.2 < \varepsilon_f \leq 1.4$ and the constant instability function below $\varepsilon_i \leq 0.2$ to fit the response to the measured data. This new simulation setup is specified in section 4.1.1 and referred to as calibration setup 2. The corresponding results are presented below.

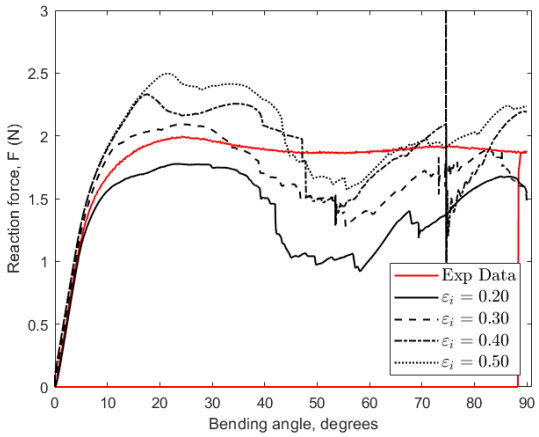

(a) Different instability values for failure function $\varepsilon_f = 1.0$.

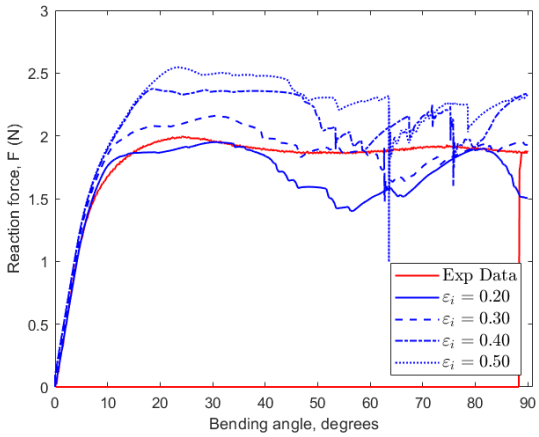

(b) Different instability values for failure function $\varepsilon_f = 1.2$.

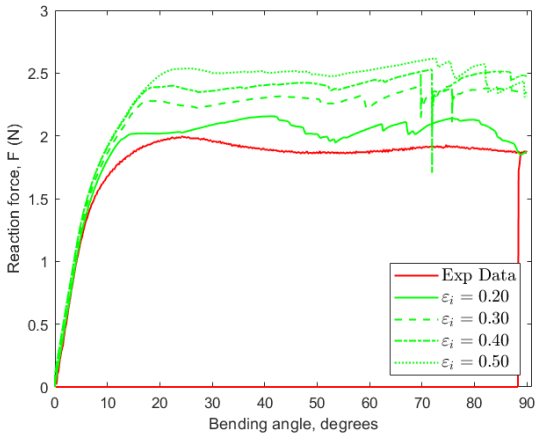

(c) Different instability values for failure function $\varepsilon_f = 1.4$.

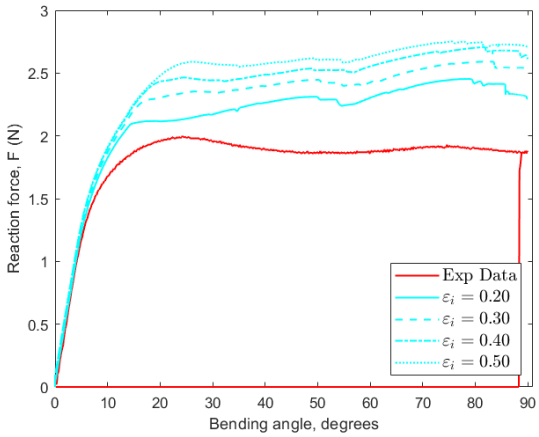

(d) Different instability values for failure function $\varepsilon_f = 1.6$.

Figure 22: Simulation results of the line folding operation of creased paperboard for calibration setup 1. In each subfigure, four simulations with different constant instability functions ε_i but the same failure function ε_f are plotted.

Calibration setup 2

In this section, the simulation results of the folding operation from the damage assumptions specified in calibration setup 2, refer to Table 8, are presented. The simulations have been structured to illustrate the effect of varying the failure and instability functions in the eGISSMO damage model during folding. The simulation results are presented in Fig. 23 below. In each subfigure, simulations with different instability values but the same constant failure function value is plotted.

Considering the subfigures in Fig. 23 in general, it is noted that using values of the instability function below $\varepsilon_i < 0.1$ yields a too low prediction of the reaction force. Moreover, and apart from what could be observed in calibration setup 1, it is noted that not only the failure function but also the instability function affects the fluctuation of the response, where using a lower instability function yields a more fluctuating response. However, the failure function still seems to affect the fluctuation of the response more than the instability function.

Considering Fig. 23(a), i.e the simulations with failure function $\varepsilon_f = 1.25$, it is

noted that the initial response is too low compared with the the measured data for all instability simulations apart from $\varepsilon_i = 0.2$. For this choice of failure function, reasonable value of the instability function seems to be $0.2 < \varepsilon_i < 0.3$, compare with Fig. 22(b). However, since the response is irregular compared with the measured data, a higher failure function should be used.

Considering Fig. 23(b), i.e simulations with a failure function of $\varepsilon_f = 1.30$, it is noted that the overall predicted reaction force is still too low for instability functions below $\varepsilon_i < 0.10$ However, for the simulations with instability functions $\varepsilon_i = 0.15$ and $\varepsilon_i = 0.20$, the overall response corresponds well. Even the initial response is in good agreement with the measured data. However, the response is still not as constant as the measured data. Hence, a higher failure function should be used.

Considering finally Figs. 23(c) and 23(d), in which higher failure functions are used, it is noted that the simulations with $\varepsilon_f = 1.40$ overall predicts the reaction force better than the simulations with $\varepsilon_f = 1.35$.

To calibrate the response further, the failure function $\varepsilon_f = 1.40$ should be used. Evaluating the simulations with $\varepsilon_f = 1.40$, it is noted that the simulation with $\varepsilon_i = 0.10$ underestimates the reaction force, whereas the simulation with $\varepsilon_i = 0.15$ slightly overestimates it. Hence, in a new calibration setup using $\varepsilon_f = 1.40$, instability functions between $0.10 < \varepsilon_i < 0.15$ should be used. The new calibration is specified in section 4.1.1 and referred to as calibration setup 3. The corresponding results are presented below.

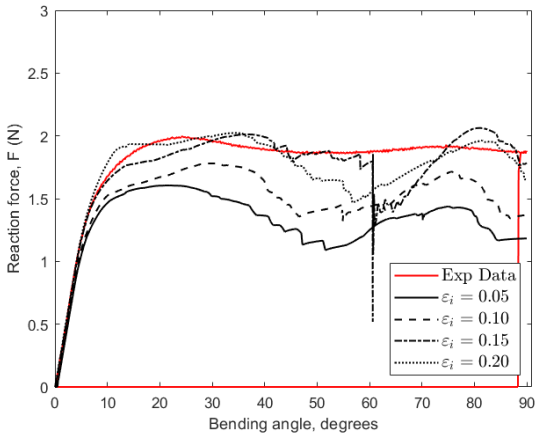

(a) Different instability values for failure function ε_f=1.25.

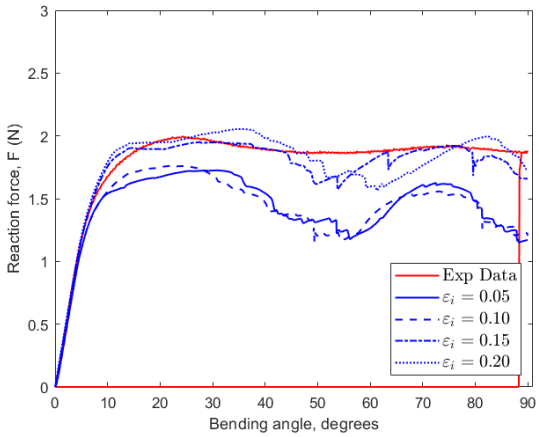

(b) Different instability values for failure function ε_f=1.30.

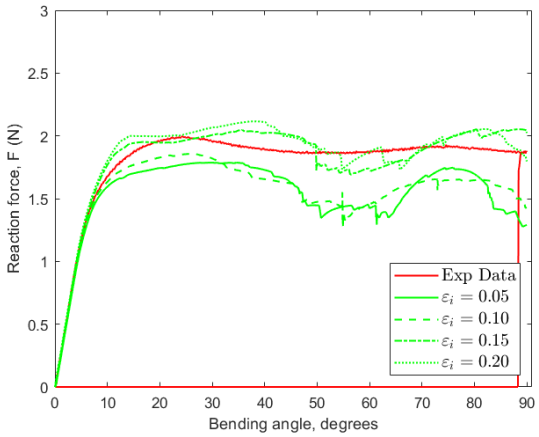

(c) Different instability values for failure function ε_f=1.35.

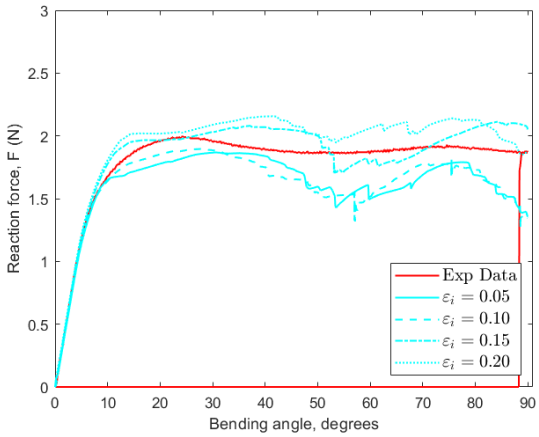

(d) Different instability values for failure function ε_f=1.40.

Figure 23: Simulation results of the line folding operation of creased paperboard for calibration setup 2. In each subfigure, four simulations with different constant instability functions ε_i but the same failure function ε_f are plotted.

Calibration setup 3

The simulation results of the folding operation from the damage assumptions specified in calibration setup 3, refer to Table 8, are presented in Fig. 24 below. In the previous calibration steps, calibration setup 1 and 2, the agreement with the measured data was easy to evaluate by simply evaluating the graphs. In this case, since the simulation curves are in closer and more precise agreement with the measured data, this method is not sufficient. Instead, a numerical evaluation is undertaken to compare the data sets. Two error measures are used. For simplicity, the measured data is called y_1 and the simulated data, for one specific choice of instability function ε_i, refer to Fig. 24, is called y_2. With these notations, the accumulated least square is calculated as

$$\text{Accumulated square error} = \sum_i (y_{1,i} - y_{2,i})^2,$$

for all data points i. Here it is emphasized that the obtained data has been structured and interpolated so that the x-values of y_1 and y_2 coincide. Apart from the accumulated

least square, the largest absolute difference between the data sets is compared. This is done by identifying the maximal $|(y_{1,i} - y_{2,i}|$ value, i.e. as

$$\text{Maximal absolute error} = \max(|(y_{1,i} - y_{2,i}|),$$

where it is emphasized that the maximal absolute error is obtained for a specific i. In Table 10 below, the accumulated square error and the maximal absolute error, as well as the bending angle at which the maximal absolute error occurs, is presented. Comparing the presented results, it is evident that the simulation with the instability function value of $\varepsilon_i = 0.14$ has the least error both in terms of accumulated square error and maximal absolute error. Hence, this is the best-calibrated simulation. To evaluate the best calibration further, other types of damage scaling than isotropic are considered. This new calibration setup is specified in section 4.1.1 and the corresponding results are presented below.

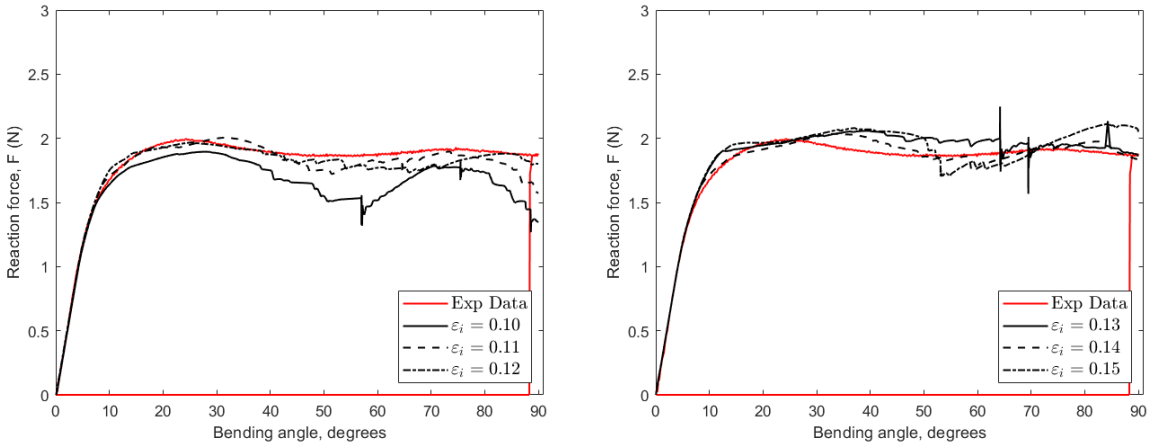

Figure 24: Simulation results of the line folding operation of creased paperboard for calibration setup 3. In the figures, six simulations with different instability functions between $0.10 \leq \varepsilon_i \leq 0.15$, but the same failure function $\varepsilon_f = 1.40$, are presented.

Table 10: Error estimations of line folding operation for calibration setup 3. Note that the simulation with the instability value $\varepsilon_i = 0.14$ has the least error both in terms of accumulated square error and maximal absolute error.

Instability value	**Acc. error**	**Max error**	**Angle at max error, degrees**
0.10	34.1764	0.5396	57.12
0.11	4.1197	0.2944	89.88
0.12	3.1136	0.1639	65.76
0.13	5.7106	0.3204	69.48
0.14	2.2192	0.1270	37.08
0.15	10.6638	0.2382	87.96

Simulation with non-isotropic damage matrices

The simulation results of the folding operation using the simulation setup specified in Table 9 are presented in Fig. 25 below. The corresponding errors, using the same measures as described in calibration setup 3 above, are presented in Table 11.

Evaluating Table 11, it is evident that the best approximation is the one in which index (5,5) in the damage matrix is put to unity. However, this index couples the stress σ_{23}. Since only a very small amount of stress is present in the CD direction, the effect of decoupling this term should be negligible. This is also what is observed - the difference in error compared with the isotropic case, refer to Table 10, is small.

Considering the other decoupled indices, it is noted that the error only gets higher. However, the error is not in this case that significant, since no calibration is made for these other types of damage coupling. What is more interesting is the shape of the curves in Fig. 25. What is evident is that many curves are unstable and fluctuating. Comparing with the isotropic simulation, all other simulations are in less agreement with the measured data. It is therefore concluded that the isotropic coupling is the best observed calibration.

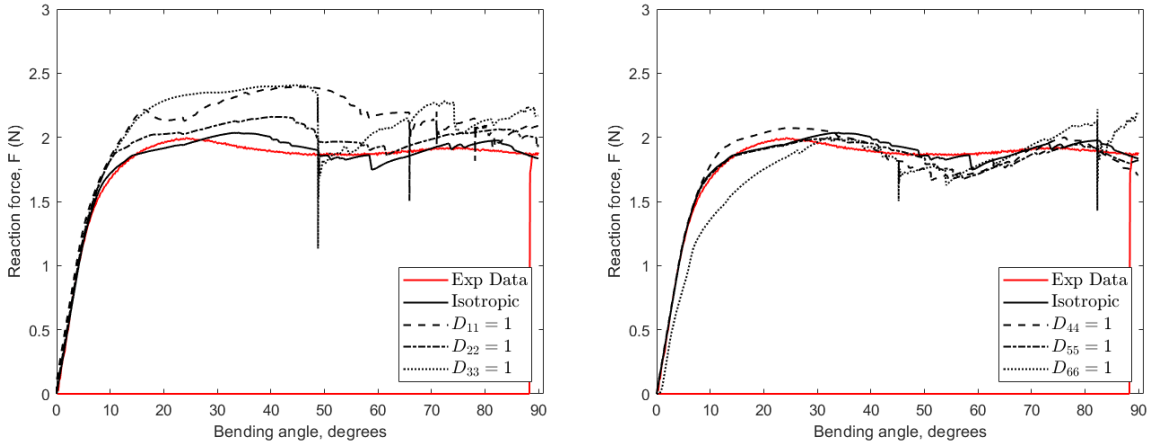

Figure 25: Simulation results for the line folding operation of creased paperboard with different damage matrices. The instability and failure function are $\varepsilon_i = 0.14$ and $\varepsilon_f = 1.40$ in all simulations.

Table 11: Error estimations of line folding operation for calibration setup 4. Note that $\varepsilon_i = 0.14$ and $\varepsilon_f = 1.40$ in all simulations. Note also that none of the simulations has a smaller error than the simulation with isotropic damage presented in calibration setup 3.

Index set to unity	**Acc. error**	**Max error**	**Angle at max error, degrees**
(1,1)	70.8319	0.5324	46.08
(2,2)	14.1196	0.2865	42.96
(3,3)	72.5977	0.5437	48.84
(4,4)	6.7015	0.2048	54.96
(5,5)	3.2204	0.2024	57.48
(6,6)	21.9531	0.4525	82.32
None	2.2192	0.2382	37.08

Evaluating the creasing operation for the best calibrated folding response
So far, only the folding operation has been considered. This is also what is the scope of this project - to obtain a better approximation of the folding through damage modeling. In calibration setup 3 it was stated that the best calibration is obtained by using the instability and failure function $\varepsilon_i = 0.14$ and $\varepsilon_f = 1.40$ with isotropic damage coupling. However, it is underlined that damage is introduced already during creasing, and it is therefore of interest to investigate how the creasing operation is affected. In Fig. 26 below, the male die force and in-plane force during creasing are plotted vs the male die displacement. In the figure, also the simulation without damage, refer to Fig. 14, is included. By comparing the simulations it is evident that there is hardly any difference between the simulation with and without damage. This is also the case when evaluating the development of the out-of-plane plastic shear and tension strain κ_{sop} and $\kappa^{(8)}$, refer to Figs. 27 and 28. It is noted that the strains in the simulation with damage is slightly more developed than for the simulation without damage. In particular, the peak value, as well as the spread of the region with higher strains, is larger for the simulation with damage.

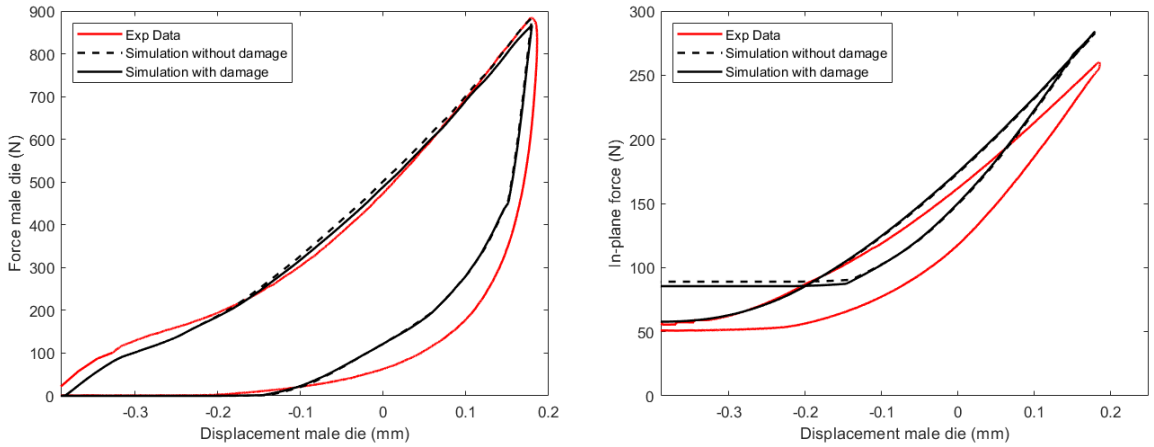

(a) Plot of reaction force of male die vs male die displacement during creasing for experimental data (red) and simulation (black).

(b) Plot of in-plane force paperboard vs male die displacement during creasing for experimental data (red) and simulation (black).

Figure 26: Force in the male die and paperboard during line creasing operation.

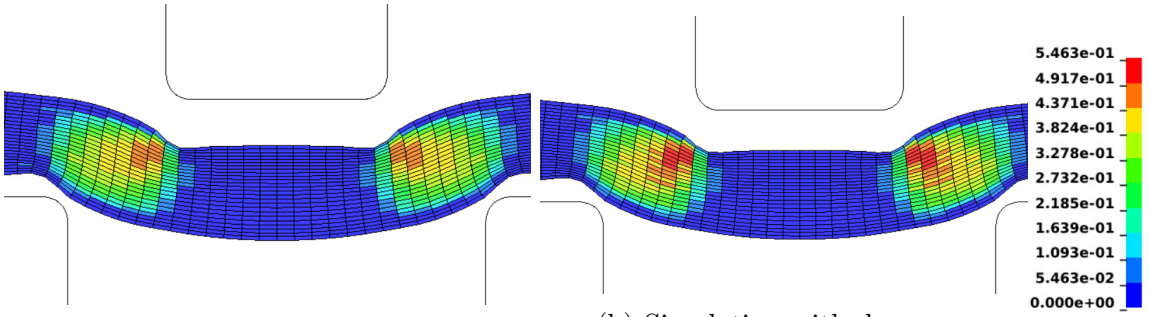

(a) Simulation without damage.

(b) Simulation with damage.

Figure 27: Plastic strain κ_{sop} at the end of the line creasing operation with and without damage. The strain is slightly more developed and has a somewhat higher peak value for the simulation with damage.

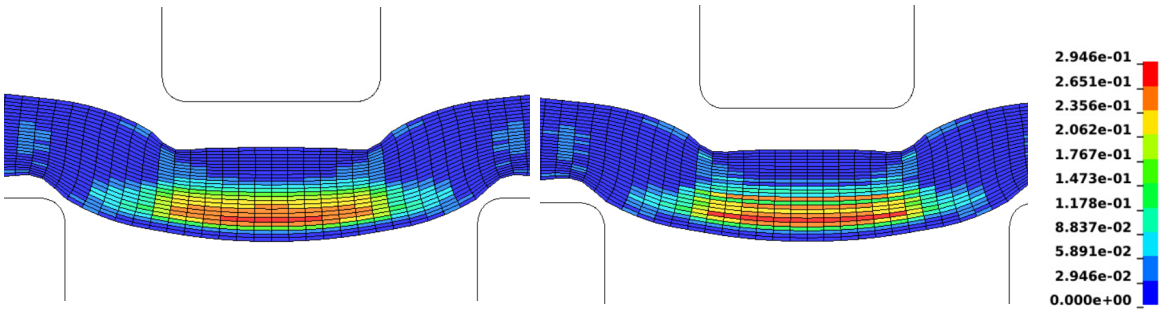

(a) Simulation without damage. (b) Simulation with damage.

Figure 28: Plastic strain $\kappa^{(8)}$ at the end of the line creasing operation with and without damage. The strain is slightly more developed and has a somewhat higher peak value for the simulation with damage.

Evaluating the folding of creased paperboard for the best calibrated folding response

In this section, the folding operation of creased paperboard for the best calibrated folding response is evaluated further. In Fig. 29, the folding response is plotted together with the simulation response with no damage. It is noted that by including damage it is possible to predict the response obtained from the measured data with high accuracy. The reaction force at the end of the folding is nearly twice as low for the simulation with damage.

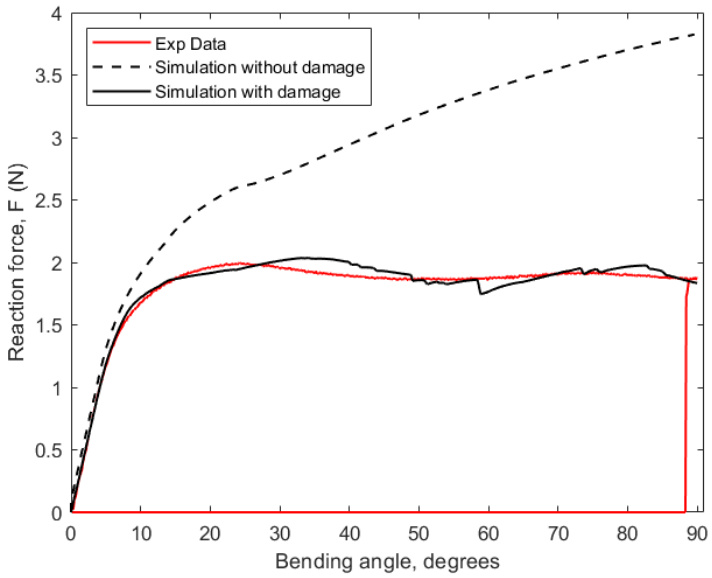

Figure 29: Folding response of creased paperboard for the best calibrated damage simulation, in which the instability and failure function is $\varepsilon_i = 0.14$ and $\varepsilon_f = 1.40$, respectively. The red curve represents the experimental data, whereas the black curves represent the simulation with and without damage.

Next, the development of the plastic out-of-plane shear and tension strain is considered. The out-of-plane plastic shear strain κ_{sop} is plotted with and without damage in Fig. 12 for bending angles of 0, 10, 20, 30, 40, 50 and 60 degrees. It is evident that the strains already in the initial part of the folding are considerably larger for

the simulation with damage. At about 30 degrees, the damage is so prominent that element erosion occurs. Since the element erosion takes place in the regions most subjected to largest strains. Hence, only elements in which the plastic strain κ_{sop} is low remain. Thus, at 60 degrees of bending, the strains are higher in the simulation without damage.

Table 12: Out-of-plane shear strain κ_{sop} at bending angles of 0, 10, 20, 30, 40, 50 and 60 degrees for isotropic damage with $\varepsilon_i = 0.14$ and $\varepsilon_f = 1.40$. Note that the same scale is used in all subfigures. Note also that the development of the plastic strains is higher in the simulation without damage.

Bending angle:	Simulation without damage:	Simulation with damage:
0°	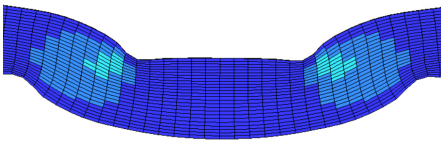	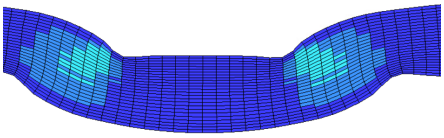
10°	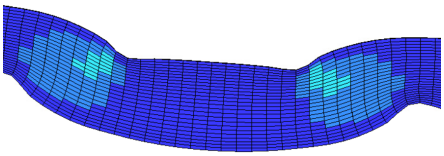	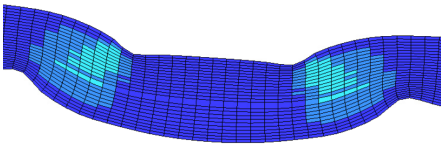
20°	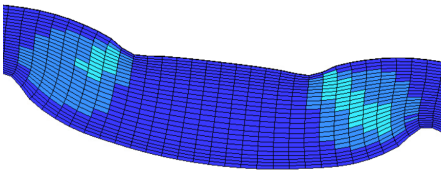	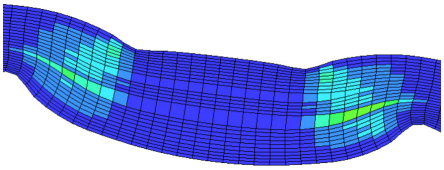
30°	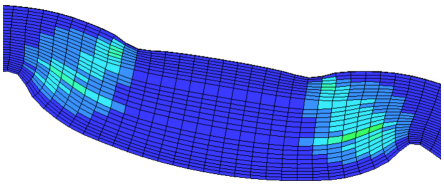	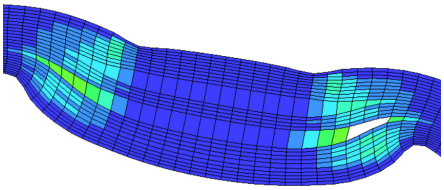
40°	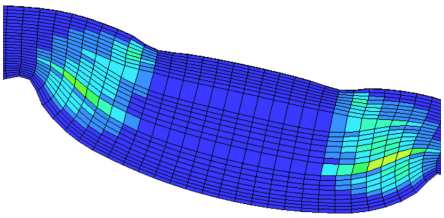	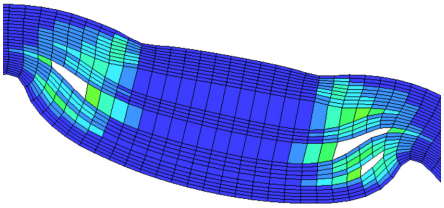
50°	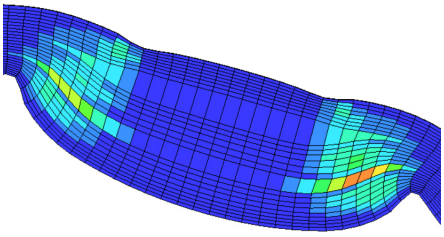	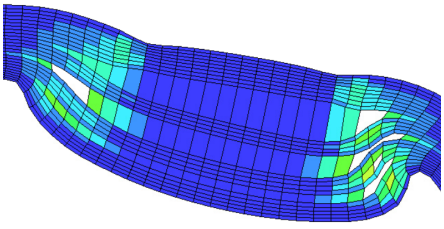
60°	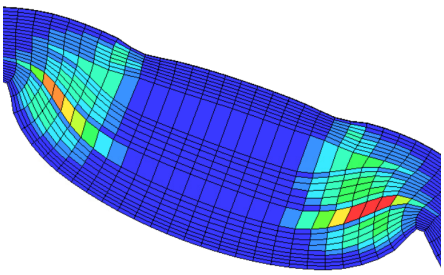	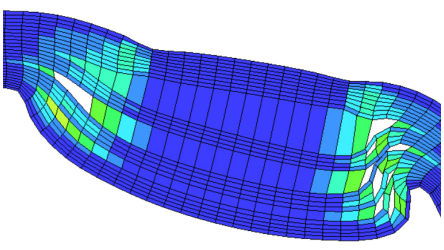

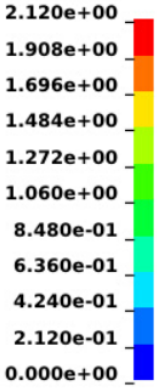

Furthermore, the simulation with damage is compared with the actual observed deformation at 60 degrees of bending, refer to Fig. 30. It is noted that the simulation predicts the micro-cracks near the clamps correctly. The simulation also predicts the asymmetry of the cracks, i.e. that there are more micro-cracks in the side nearest to the clamps. However, the erosion of material in the middle of the creased zone is not observed in the simulation.

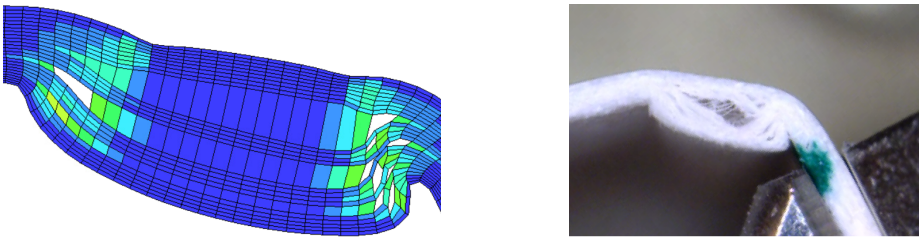

Figure 30: Comparison of the simulated response with the actual deformation at a bending angle of 60 degrees. The formation of cracks near the clamps as well as the asymmetry of the cracks is predicted by the simulation. The simulation does not predict the well defined delamination in the middle of the creased zone.

Comparing finally the out-of-plane plastic tension strain $\kappa^{(8)}$ for the simulation with and without damage for bending angles of 0, 10, 20, 30, 40, 50 and 60 degrees, refer to Table. 13, it is noted that significantly higher strains develop in the simulation with damage. It is underlined that this observation holds also for a bending angle of 60 degrees, at which element erosion has occurred. This is because the damage is localised in regions in which the out-of-plane plastic shear strain is high, not the out-of-plane plastic tension strain. Hence, elements with a high out-of-plane tension strain are not eroded.

Table 13: Out-of-plane tension strain $\kappa^{(8)}$ at bending angles of 0, 10, 20, 30, 40, 50 and 60 degrees for isotropic damage with $\varepsilon_i = 0.14$ and $\varepsilon_f = 1.40$. Note that the same scale is used in all three subfigures. Note also that the development of the plastic strains is higher than for the simulation without damage.

Bending angle:	Simulation without damage:	Simulation with damage:
0°	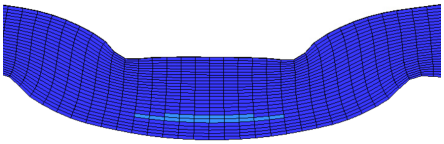	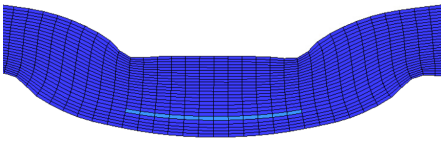
10°	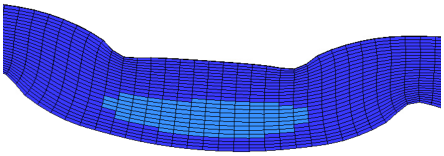	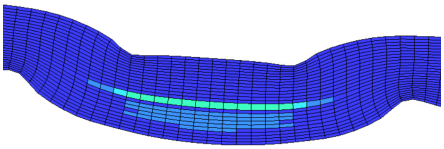
20°	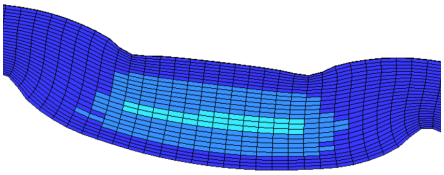	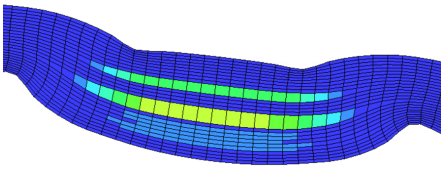
30°	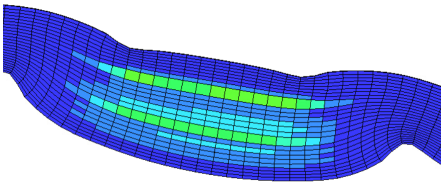	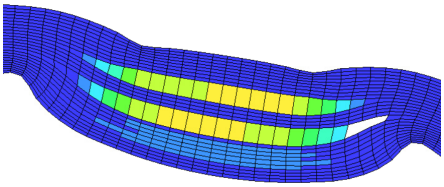
40°	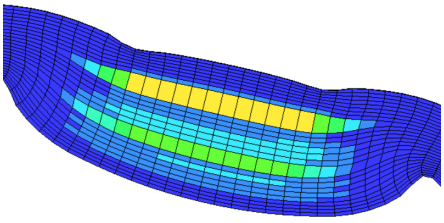	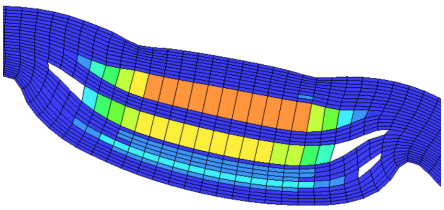
50°	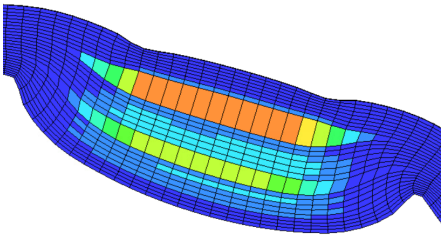	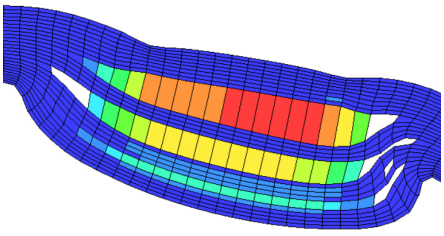
60°	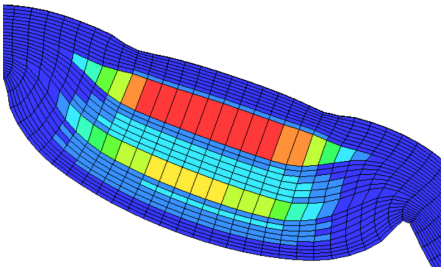	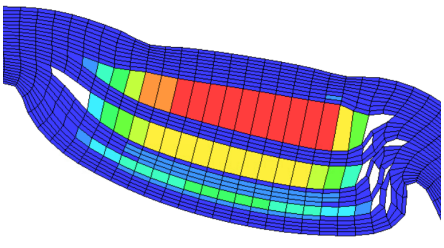

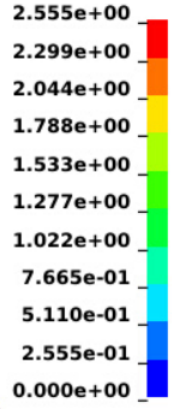

Evaluating folding of uncreased paperboard for the best calibrated folding response

In this section, the folding of uncreased paperboard for the best calibrated folding response is evaluated. The simulation response with and without damage, as well as the folding of creased paperboard, is depicted in Fig. 31. It is noted that for the folding of uncreased paperboard, the simulation predictions with and without damage are identical up until 45 degrees of bending. After this, the simulation with damage predicts the reaction force slightly lower than the simulation without damage. Thus, the simulation with damage is for higher bending angles in less agreement with the measured data. However, the difference between the simulation predictions is small. The RCS value is calculated to

$$\text{RCS} = \frac{P^{max}_{b,creased,0<\theta<30}}{P^{max}_{b,uncreased,0<\theta<30}} = \frac{1.95}{4.4} = 0.44,$$

which is in rather good agreement with the measured data, for which RCS = 0.39. The relative difference is calculated to $(0.44 - 0.39)/0.44 = 11\%$. The accuracy is hence improved by a factor of $36/11 = 3.2$, compared with the simulation without damage. The RCS values for the measured data and the simulations with and without damage are summarized in Table 14 below.

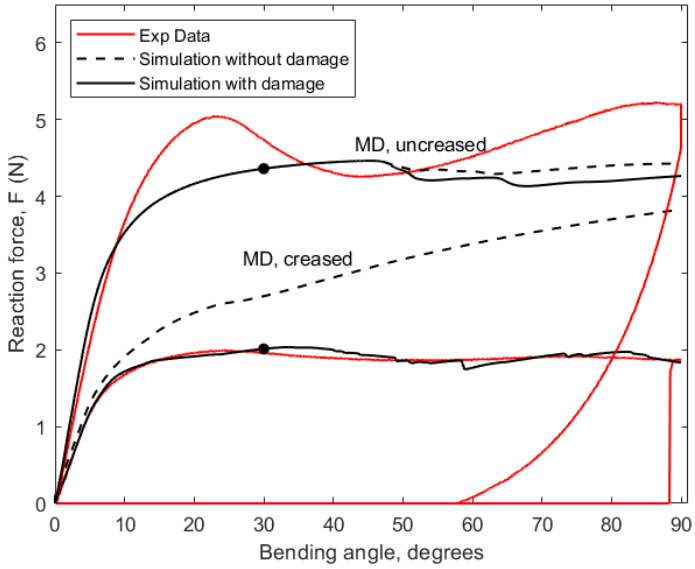

Figure 31: Folding response of creased and uncreased paperboard for the best calibrated damage simulation, which have the instability and failure function $\varepsilon_i = 0.14$ and $\varepsilon_f = 1.40$. The red curves represent the experimental data whereas the black curves represent the simulation with and without damage.

Table 14: RCS for measured data and simulation with and without damage.

Experiment/simulation	**RCS**	**Relative difference with measured data (%)**
Measured data	0.39	0
Simulation without damage	0.61	36
Simulation with damage	0.44	11

4.2 Calibrating folding of creased paperboard by using out-of-plane plastic tension strain as driving history variable

In this section, the results of the creasing and folding operation simulated with damage, using the out-of-plane shear strain as the driving history variable, is presented. The simulation setup is presented in section 4.2.1, and the corresponding results are presented in section 4.2.2.

4.2.1 Method

In the second approach to calibrate the folding response of creased paperboard, the driving history variable is chosen as

$$\Delta HIS = \kappa^{(8)}$$

With the history variable chosen, what remains is to choose the instability and damage functions ε_i and ε_f and the damage matrix present in the stress coupling, refer to (12).

A first calibration setup, identical with calibration setup 1, is made in which a total number of 16 simulations are carried out with different instability and failure functions, ε_i and ε_f. The stress coupling is specified to be isotropic. The calibration is referred to as *calibration setup 1* and specified in Table 15 below.

As calibration setup 1 yields result that are not in sufficient agreement with the measured data, a new calibration setup is made. It was concluded in the evaluation of the results that new simulations should be undertaken with the instability and failure function below $\varepsilon_i \leq 0.20$ and $\varepsilon_f \leq 1.0$. Also in this calibration, the stress coupling is specified to be isotropic. The calibrations are referred to as *calibration setup 2* and specified in Table 15 below.

Table 15: The instability and failure function for different calibration setups. The black circles and blue squares refer to calibration setup 1 and 2, respectively.

ε_f \ ε_i	**0.05**	**0.10**	**0.15**	**0.20**	**0.30**	**0.40**	**0.50**
0.40	■	■	■	■			
0.60	■	■	■	■			
0.80	■	■	■	■			
1.00	■	■	■	●	●	●	●
1.20				●	●	●	●
1.40				●	●	●	●
1.60				●	●	●	●

Finally, to obtain more insight in the folding response using the plastic out-of-plane strain $\kappa^{(8)}$ as the driving history variable, different formats of the damage matrix are investigated. The investigation is completely similar with the investigation using κ_{sop} as the driving history variable, refer to Table 9.

4.2.2 Results

In this section, the results from the simulation incorporating damage with the out-of-plane tension strain $\kappa^{(8)}$ as the driving history variable, refer to section 4.2.1, is presented. To start with, only the folding results of creased paperboard is presented.

Table 16: Investigation of different damage matrices. Note that the same instability and failure functions are used in all simulations.

Simulation nr.	**Index set to unity**	ε_i	ε_f
1	(1,1)	0.20	1.0
2	(2,2)	0.20	1.0
3	(3,3)	0.20	1.0
4	(4,4)	0.20	1.0
5	(5,5)	0.20	1.0
6	(6,6)	0.20	1.0

First, the folding results from calibration setup 1, 2 and 3 are presented. For one of the calibrations, the strains and deformed shape during folding of creased paperboard is presented.

Calibration setup 1

The simulation results of the folding operation from the damage assumptions specified in calibration setup 1, refer to Table 15, are presented in Fig. 32 below. In each subfigure, simulations with different instability functions but the same failure function are plotted.

It is evident that all simulations presented in Fig. 32 exhibit a very similar response. It is particularly noted that all simulations are in poor agreement with the measured data - the reaction force at the load cell is highly overestimated. It is also observed that none of the simulations exhibits a response shape that is constant and thus in agreement with the measured data. Instead, the reaction force increases continuously with the bending angle, and a response that is more similar to the simulation without damage, refer to Fig. 18, is obtained.

The biggest difference between the simulations can be observed at the initial phase of the operation, at bending angles of about 10 degrees. The simulations undertaken with the failure function $\varepsilon_f = 1.0$, refer to Fig. 32a, have the best agreement with the measured data at this phase, whereas the simulations with a higher failure function is in poorer agreement with the measured data. In fact, the poorer agreement can be observed also for the overall response, and it is then concluded that the simulation with the best agreement with the measured data is the one in which the instability and failure function is chosen as $\varepsilon_i = 0.20$ and $\varepsilon_f = 1.0$, i.e. the simulation with the most damage included.

From the observations above, it is tempting to make a new calibration setup in which the failure and instability function is further decreased below $\varepsilon_i = 0.20$ and $\varepsilon_f = 1.0$. However, it is noted that the initial response for this simulation is in good agreement with the measured data. Hence, lowering the instability or function further would imply the risk of a poorer fit at the initial stage. However, the case is worth investigating. Hence, a new simulation setup using $\varepsilon_i \leq 0.20$ and $\varepsilon_f \leq 1.0$ is made. This new calibration setup is further specified in section 4.2.1 and refereed to as calibration setup 2. The results are presented below.

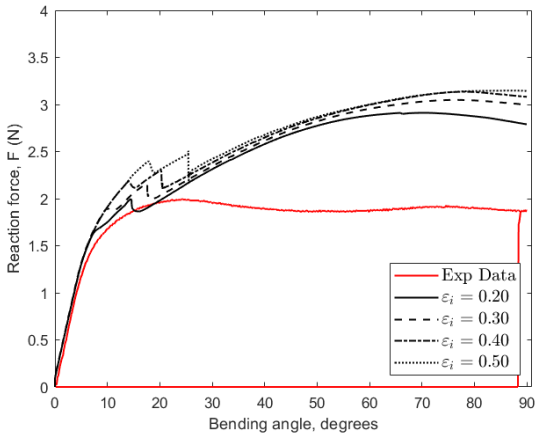

(a) Different instability values for failure function ε_f=1.0.

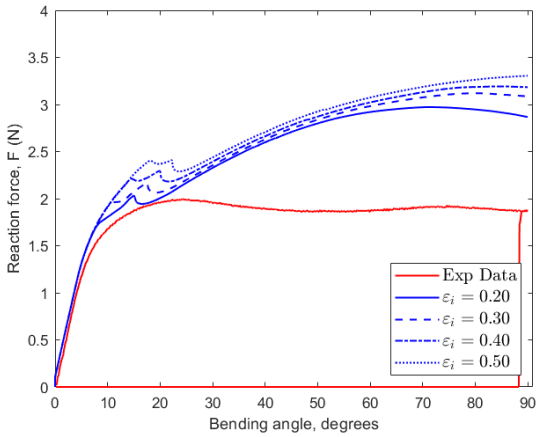

(b) Different instability values for failure function ε_f=1.2.

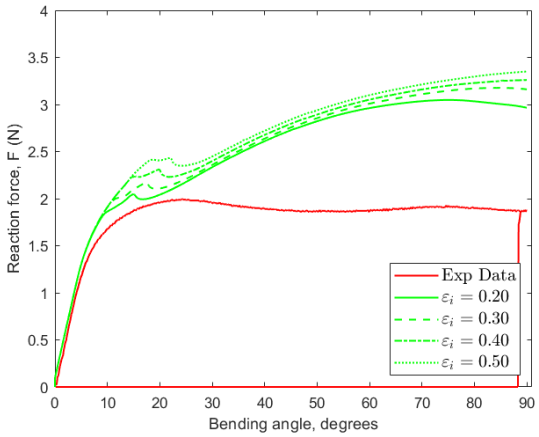

(c) Different instability values for failure function ε_f=1.4.

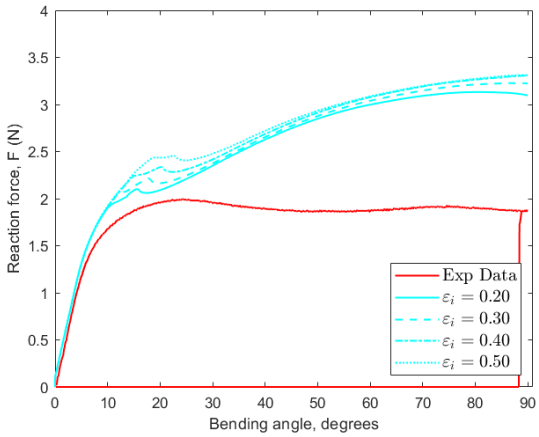

(d) Different instability values for failure function ε_f=1.6.

Figure 32: Simulation results of the line folding operation for calibration setup 1. In each subfigure, four simulations with different constant instability functions ε_i but the same failure function ε_f are plotted..

Calibration setup 2

The simulation results of the folding operation from the damage assumptions specified in calibration setup 2, refer to Table 15, are presented in Fig. 33 below. Evaluating the figure, it is noted that the possibility to affect the response by decreasing the failure function is limited. The response is in general quite hard to predict. For example, the reaction force is predicted lower for the failure function $\varepsilon_f = 1.0$ than $\varepsilon_f = 0.8$, compare Figs. 33c and 33d. Moreover, in for these failure functions the reaction force is lower for $\varepsilon_i = 0.15$ than for $\varepsilon_i = 0.05$. Hence, using the out-of-plane tension plastic strain as the driving history variable alone does not seem to be a good strategy for calibrating the folding response with the measured data. However, to make a final attempt, different damage matrices than isotropic are considered. This calibration setup is specified in section 4.2.1 and the results are presented below.

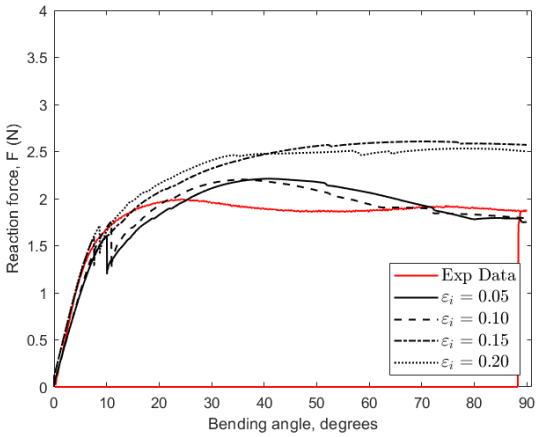

(a) Different instability values for failure function $\varepsilon_f = 0.4$.

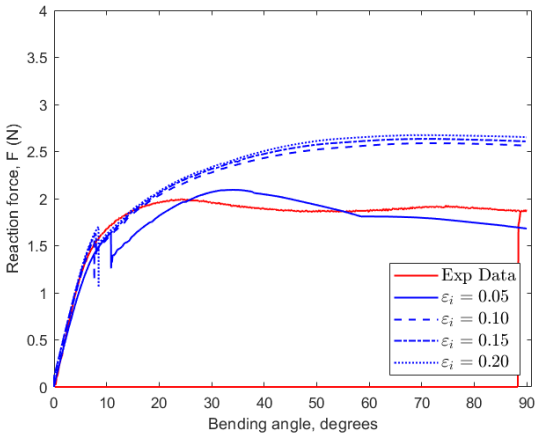

(b) Different instability values for failure function $\varepsilon_f = 0.6$.

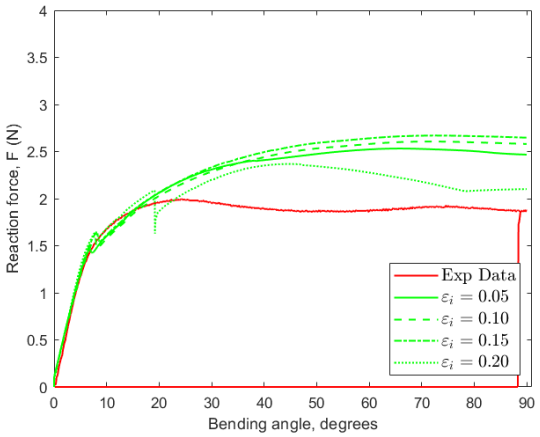

(c) Different instability values for failure function $\varepsilon_f = 0.8$.

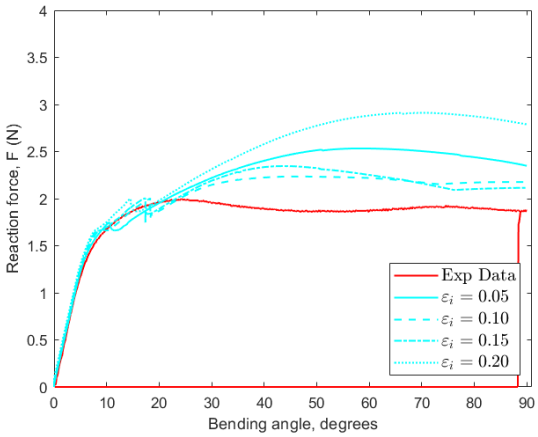

(d) Different instability values for failure function $\varepsilon_f = 1.0$.

Figure 33: Simulation results of the line folding operation for calibration setup 2. In each subfigure, four simulations with different constant instability functions ε_i but the same failure function ε_f are plotted.

Simulations with non-isotropic damage matrices

The simulation results of the folding operation using the simulation setup specified in Table 16 are presented in Fig. 34 below. Evaluating the figure, it is evident that all responses are similar except the simulation in which index (3,3) in the damage matrix is set to unity. However, even if this simulation is closer to the measured data, it shows a more unstable behaviour.

As none of the calibrations so far have shown promising behaviour, no further calibrations are made. The deformed shape during folding is however further considered. Below, the deformed configuration and out-of-plane tension strain for the folding of creased paperboard using instability and failure of $\varepsilon_i = 0.20$ and $\varepsilon_f = 1.0$ is depicted.

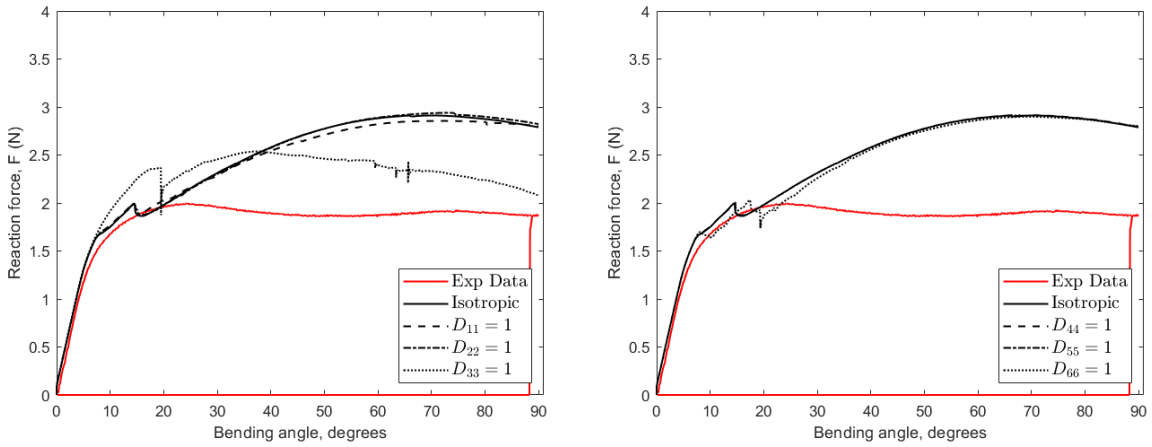

Figure 34: Simulation results for the line folding operation of creased paperboard with different damage matrices for $\varepsilon_i = 0.20$ and $\varepsilon_f = 1.0$.

Evaluation of the deformed shape during folding

The deformed configuration and out-of-plane plastic tension strain $\kappa^{(8)}$ for the simulation with instability and failure function $\varepsilon_i = 0.20$ and $\varepsilon_f = 1.0$ is presented in Fig. 35, in which also the simulation without damage as well as the actual deformation are depicted for comparison. In the figure, $\kappa^{(8)}$ is plotted for at 60 degrees of bending. It is observed that the strain, and by implication the element erosion, is concentrated in the middle of the delaminated zone of the paperboard. Due to the element erosion, the strains are lower in the simulation with damage. It is also observed that the simulation, compared with the actual deformation, captures the delamination in the creased zone but not the cracks near the clamps.

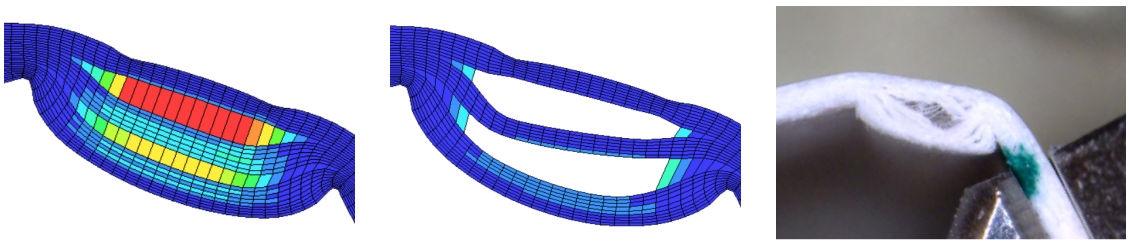

Figure 35: Out-of-plane tension strain $\kappa^{(8)}$ at 60 degrees of bending without (left) and with (right) damage. For the simulation without damage, the damage coupling is isotropic and the instability and failure function is $\varepsilon_i = 0.20$ and $\varepsilon_f = 1.0$, respectively.

5 Simulation of uniaxial tests

As has been observed in the previous section, two deformation mechanisms that have been investigated in the folding operation are the out-of-plane shear and tension. Hence, it is of interest to also perform uniaxial tests for these two deformation mechanisms. The paperboard response is simulated using a model with a single element as well as with multiple elements. The simulation of the uniaxial out-of-plane shear test is described in section 5.1, whereas the simulation of the uniaxial out-of-plane tension test is described in section 5.2.

5.1 MD-ZD shear test

In this section, the simulation setup and results of a MD-ZD shear test is presented. The simulations are undertaken both without damage and for the best calibrated damage simulation of the folding of creased paperboard. The simulation setup is described in section 5.1.1 and the corresponding results are presented in sections 5.1.2 and 5.1.3.

Finally, the MDZD-tension test is presented for the same calibration. The ZD-tension test is not carried out since no shear strains develop in that case.

5.1.1 Method

The out-of-plane shear, or MD-ZD shear, is a potential important deformation mechanism in the folding operation. It is therefore of interest to investigate the uniaxial response of this type of loading, as well as the influence of the element size. A fixed geometry with an area of 10x10 mm and a thickness of 0.4 mm is considered. The model is fixed in all nodes at the bottom, and the loading is introduced as a prescribed displacement set to 5 mm in the MD-direction at the nodes on the upper surface of the model, refer to Fig. 36. This means that the normalised prescribed displacement, with respect to the initial length of the model, becomes $\bar{u} = 5/10 = 0.5$. The geometrical quantities are summarized in Table 17 below.

Multiple simulations are carried out in which the region is meshed with different number of elements through the thickness. The simulation setup is specified in Table 18. To mimic the response during the line creasing and folding operation, plasticity is assumed to localise in only one of the elements through the thickness. This is accomplished by slightly lowering the limit of the distance to the yield surface $K_o^{(9)}$ from 2.28 MPa to 2.10 MPa in the element in which plastic deformation is supposed to occur. Observe that the yield stress is expressed in terms of the Kirchhoff stress.

Table 17: Geometrical properties of the paperboard model used in the MD-ZD shear tests.

Width (mm)	Length (mm)	Thickness (mm)	Presc. displacement (mm)	Presc. direction
10	10	0.4	5	MD

Table 18: Simulation setup for uniaxial MD-ZD shear test.

Simulation nr.	Elements through the thickness
1	1
2	3
3	25

Figure 36: Simulation models with one and three elements through the thickness.

5.1.2 Results for simulation without damage

In this section, the simulation results of the paperboard material response to uniform loading in the MD-ZD direction is presented. The simulations have been carried out using the simulation setup described in section 5.1.1. Three simulations have been carried out, in which the geometry was modelled using 1, 3 and 25 elements through the thickness, respectively.

As stated in section 5.1.1, the distance to the yield surface $K_o^{(9)}$ and $K_o^{(10)}$ was changed in order for the plastic deformation to localise in one element only. The localisation is indeed observed in the simulations, as seen in Fig. 37. The resultant Kirchoff stress response in the localised element, as well as in the other elements, is presented in Fig. 38(a).

The results of the simulations are depicted in Fig. 38(b). It is noted that the number of elements used to model the region has a significant impact on the response of the material. Since this test is not a uniform MD-ZD shear test, but a test that involves more than one stress component, it is hard to predict the response. For example, apart from the MD-ZD shear stress, dilatation is observed in the material.

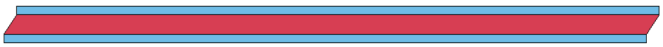

Figure 37: The plastic response is localised in one of the elements.

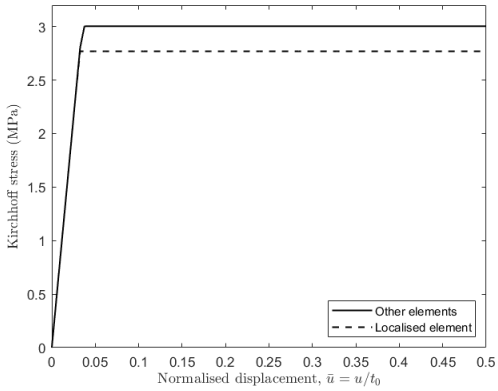

(a) Kirchoff stress in the localised and the other elements. The yield stress has been lowered in all elements but the localised in order for the plastic response to take place in this element only.

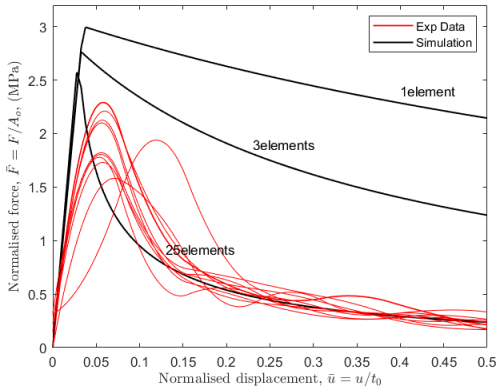

(b) Experimental data (red) and simulation (black) of shear tests in the MD-ZD direction. The force F is normalised with the initial area A_o, whereas the displacement u is normalised with the initial thickness t_o. Simulation results have been obtained using 1, 3 and 25 elements through the thickness.

Figure 38: Simulation results of MD-ZD shear test.

5.1.3 Results for simulation with damage

To conclude the result section, the MD-ZD shear test is carried out with damage included according to the best calibration. The results are depicted in Fig. 39 below. The response obtained with damage is softer than the without. For the simulation with damage and 25 elements through the thickness, the shear strain in the localised element is so high that the element is eroded. It is observed that the prediction of the normalised force is too low compared with the measured data.

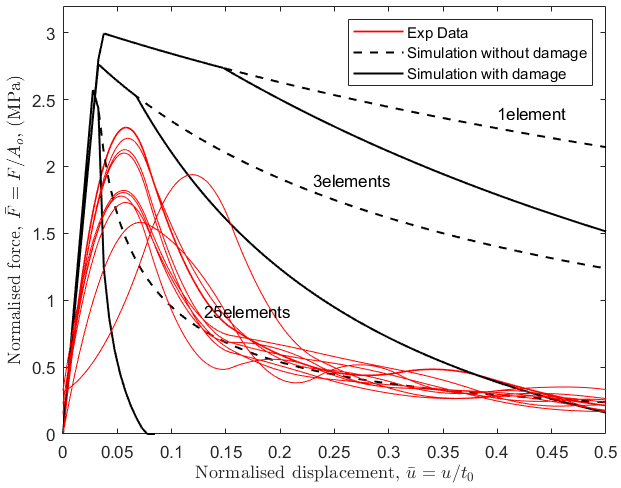

Figure 39: Experimental data (red) and simulation (black) of shear tests in the MD-ZD direction. The force F is normalised with the initial area A_o, whereas the displacement u is normalised with the initial thickness t_o. Simulation results have been obtained using 1, 3 and 25 elements through the thickness.

5.2 ZD-tension test

In this section, the simulation setup and results of a ZD-tension test are presented. The simulations are undertaken only without damage, since for the best calibrated damage simulation of the folding of creased paperboard the damage is introduced in the shear strain direction. The best calibrated damage will therefore not change the results of the ZD-test. The simulation setup is described in section 5.2.1 and the corresponding results are presented in section 5.2.2.

5.2.1 Method

The out-of-plane tension, or ZD-tension, is also a potentially important deformation mechanism in the folding operation. It is therefore of interest to investigate the uniaxial response of this type of loading, as well as the influence of the element size. The same fixed geometry, as described in section 5.1.1 above, is adopted, refer to Fig. 36. The model is fixed in all nodes at the bottom, and the loading is introduced as a prescribed displacement of 0.6 mm in the ZD-direction at the nodes on the upper surface of the model. This means that the normalised prescribed displacement, with respect to the initial thickness of the model, becomes $\bar{u} = 0.6/0.4 = 1.5$. The geometrical quantities are summarized in Table 19 below.

Multiple simulations are carried out in which the region is meshed with different number of elements through the thickness. The simulation setup is specified in Table 20. To mimic the response during the line creasing and folding operation, plasticity is assumed to localise in only one of the elements through the thickness. This is accomplished by slightly lowering the limit of the distance to the yield surface $K_o^{(8)}$ from 0.439 MPa to 0.435 MPa in the element in which plastic deformation is supposed to occur. The initial yield surface in the ZD - MD-ZD stress space is depicted in Fig. 40 below.

Table 19: Geometrical properties of the paperboard model used in the ZD-tension simulation.

Width (mm)	Length (mm)	Thickness (mm)	Presc. displacement (mm)	Presc. direction
10	10	0.4	0.6	ZD

Table 20: Simulation setup for uniaxial MD-ZD shear test.

Simulation nr.	**Elements through thickness**
1	1
2	3
3	25

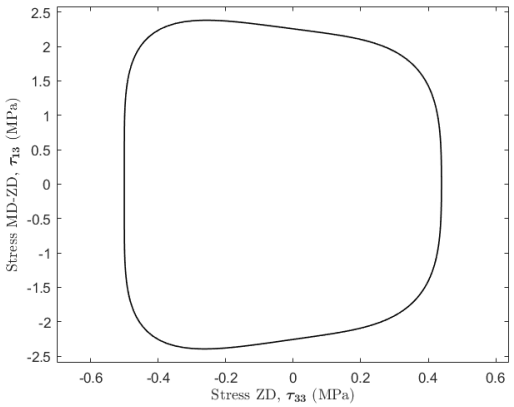

Figure 40: Initial yield surface in the ZD - MD-ZD stress space. Note the initial distance to the yield surface.

5.2.2 Results

For the simulation of the uniaxial test in the ZD-direction, three simulations have been carried out, in which the geometry was modelled using 1, 3 and 25 elements through the thickness. The distance to the yield surface $K_o^{(8)}$ was changed for the plastic deformation to localise in one element only. In Fig. 41, the final deformed configuration of the model with three elements through the thickness is presented. From this figure, the localisation is indeed observed. In Fig. 42(a), the resultant Kirchoff stress response in the localised element, as well as in the other elements, is presented. It is observed that ideal plasticity is indeed present in terms of the Kirchhoff stress tensor. In Fig. 42(b) the normalized force-displacement graphs are plotted for the simulations undertaken. From the figure, it is evident that the number of elements through the thickness have a significant impact on the response. To understand why, it is first noted that ideal plasticity is assumed in terms of the Kirchhoff stress, as already explained and depicted in Fig. 42(a). It is also emphasized that the normalised force and displacement is the overall force and displacement, i.e. not the displacement of the single element. Moreover, it is again emphasized that plastic deformation occurs in one element only. Using these observations, assuming that all stress is distributed to the localised element, and denoting the number of elements through the thickness by n, the normalized force can approximately be calculated as

$$F = \int \sigma dA = \int \hat{\sigma} d\hat{A} = \int \frac{\hat{\tau}}{\hat{J}} d\hat{A} \approx \frac{\tau^o}{\hat{V}/\hat{V}_o}\hat{A} = \frac{\tau^o}{(\hat{A}\hat{t})/(\hat{A}_o\hat{t}_o)}\hat{A} = [A_o \approx \hat{A}_o] = \frac{\tau^o A_o}{\hat{t}/\hat{t}_o}$$

$$\Rightarrow \frac{F}{A_o} = \frac{\tau^o}{(\hat{t}_o + u)/\hat{t}_o} = \frac{\tau^o}{1 + u/\hat{t}_o} = [\hat{t}_o = t_o/n] = \frac{\tau^o}{1 + nu/t_o}$$

$$\Rightarrow \bar{F} = \frac{\tau^o}{1 + n\bar{u}}, \tag{18}$$

in which the hat symbol denotes the element in which plasticity is localised. Note that τ^o is used to denote the yield stress in the localised element. Comparing (18) with the obtained simulations results, see Fig. 43, reveals that (18) well describes how the response varies with the number of elements used through the thickness.

Figure 41: The plastic response is localised in one of the elements.

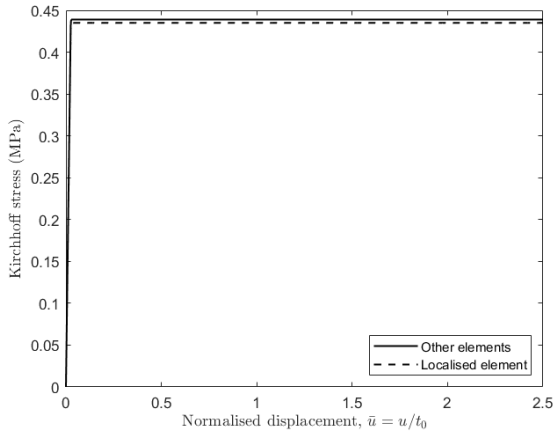

(a) Kirchoff stress in the localised and in the other elements. The yield stress has been lowered in all elements but one in order for the plastic response to take place in one element only.

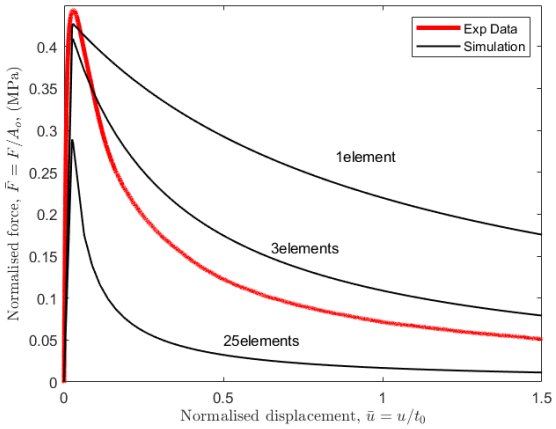

(b) Experimental data (red) and simulation results (black) of tension tests in the ZD-direction. The force F is normalised with the initial area A_o, whereas the displacement u is normalised with the initial thickness t_o.

Figure 42: Simulation results of ZD-tension test.

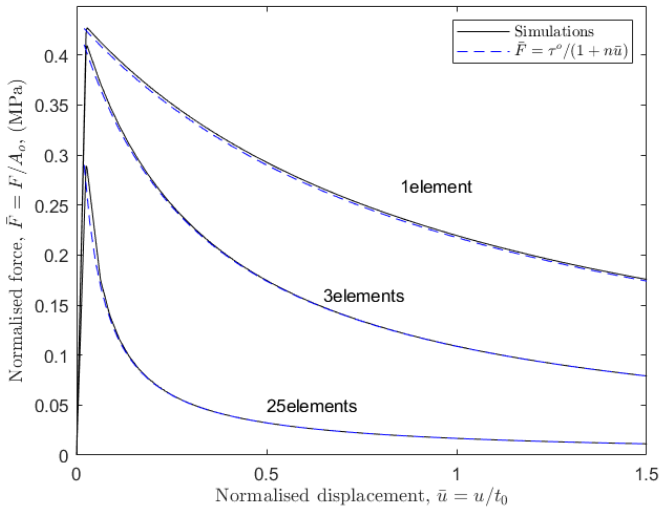

Figure 43: Comparison of the simulation results (black) with the derived expression (18) (blue) using 1, 3 and 25 elements through the thickness.

6 Conclusions and future work

In this section, the creasing and folding simulations with and without damage, as well as the uniaxial tests, are evaluated and discussed. Finally, some aspects that can be further investigated are proposed.

Simulation without damage
Starting by evaluating the simulation without damage, it was concluded that the folding of creased paperboard is highly overestimated. The measured data exhibit a constant reaction force after 10 degrees of bending whereas the simulation predicts the reaction force to increase continuously. This implies the need for a damage model. Some delamination is observed in the simulation at 60 degrees of bending, but the overall deformation is not well in agreement with the actual deformation of the specimen. Considering finally the folding of uncreased paperboard, the RCS value was calculated to 0.61.

Evaluating the MD-ZD shear test, the simulation with 25 elements through the thickness is in best agreement with the experimental data. Considering instead the ZD tension test, 3 elements through the thickness is closer to the experimental data. However, by observing the deformation during folding, it is not entirely clear how many elements through the thickness that are affected. The ply is indeed modelled with 25 elements through the thickness. However, the number of elements active in the delamination may be fewer.

Simulation with damage - out-of-plane plastic shear as driving history variable
For the calibration using the shear strain as the driving history variable, a satisfying fit with the measured data was obtained by using the instability and failure function $\varepsilon_i = 0.14$ and $\varepsilon_f = 1.40$. Both the accumulated and absolute error was very low.

Considering the creasing operation, and comparing it with the simulation without damage, the difference in in-plane force and male die force response is marginal. The creasing can be considered as a critical test of the damage model, and since the incorporation of damage does not worsen the creasing simulation, which already predicts the measured data in terms of male die and in-plane force rather correctly, the critical test is passed. Moreover, considering the out-of-plane strains during creasing, it was observed that the peak strains are higher and the region with higher strains is larger compared to the model without damage. However, the difference is small and the strains are only slightly more developed in the simulation with damage. Hence, also in terms of the strains, the creasing is rather unaffected by the introduction of damage.

Evaluating next the out-of-plane strains in the folding of creased paperboard, it was noted that the strains are much higher than the simulation without damage. The strains are so large that element erosion occurs. However, because of this, the simulation is able to predict the micro-cracks that form near the clamps, as well as the asymmetry of these cracks. The delamination in the out-of-plane direction is yet not entirely captured by the simulation. However, the overall deformation is still in good agreement with the actual deformation of the specimen. The deformed configuration validates that the calibration, which was made for the response of the reaction force at the load cell - not for the deformation, is physically sound.

Considering finally the folding of uncreased paperboard, it was noted that the

introduction of damage only had a negligible effect on the simulation results. Also the folding of uncreased paperboard can be thought of as a critical test of the damage model, since introducing damage have the effect of softening the material and thus lowering the predicted reaction force. For the case of uncreased paperboard, the folding response is already predicted too low. Hence, the best scenario, in this case, is that the simulation with damage has a low impact on the behaviour, and this is exactly what is observed. The negligible effect on the folding of uncreased paperboard is a second validation of the calibration. This is confirmed by the RCS value, which was calculated to 0.44 for the simulation with damage. This is in good agreement with the measured data, for which RCS was calculated to 0.39.

Simulation with damage - out-of-plane plastic tension as driving history variable

Evaluating the calibration in which the tension strain was chosen as the driving history variable, no good fit to the measured data was obtained. The conclusion from calibration setup 1 and 2 is that the possibility to calibrate the reaction force response by changing the failure function is limited. In calibration setup 2 a very unstable behaviour was obtained. For example, it was observed that a lower failure function yielded a higher prediction of the reaction force.

The damage takes place very locally, in the middle of the creased region. The delamination is in good agreement with the actual deformation. However, the micro-cracks near the clamps are not predicted by the simulation.

Summary

To summarize the results, it is concluded that it is possible to obtain a good fit of the folding of creased paperboard by using damage simulation by eGISSMO in LS-Dyna. Considering the two approaches for incorporating damage, it is noted that the prediction of the folding of creased paperboard is easier to control and calibrate by using the out-of-plane plastic shear strain as the history variable. Moreover, the agreement with the measured data is much better in this case.

By evaluating the deformed responses for the two approaches, it was observed that using the shear strain as the history variable, the micro-cracks near the clamps are captured, whereas using the tension strain as the history variable, the delamination is captured. Hence, the conclusion is that the out-of-plane shear strain seems to have a larger impact on the folding of creased paperboard in the MD-direction than the out-of-plane tension strain. This is also observed in the response obtained by using the tension strain as the history variable, in which much lower instability and failure functions were needed to predict the response with some accuracy. The fact that larger damage is needed implies that the folding response is more sensitive for damage in other regions than those where the out-of-plane tension strain is dominant. More specifically, the first damage approach shows that damage should preferably be introduced in regions where the out-of-plane shear strain is predominant.

Future work

The results show that it is sufficient to use the out-of-plane shear strain as the driving history variable to calibrate the folding response. However, only the micro-cracks near the clamps, and not the element erosion in the delaminated zone, is predicted. To capture the full deformation pattern, the two approaches of including damage considered in this work could be combined. Based on the results obtained in this work, it should be sufficient to include only a small amount of damage in the out-of-plane tension direction to capture the full deformation pattern.

Furthermore, it is noted that damage modeling is a calibration procedure. In future work, it would be interesting to investigate whether it is possible to generalize the damage formulation to narrow the calibration needed. One idea is to see if the damage could be determined based on the resulting out-of-plane shear for the simulation without damage. In that case, simulations could first be conducted without damage. Then, based on the magnitude of the out-of-plane shear strain, correct instability and failure functions could be determined. To find such relations, and to further validate the work done here, other paperboard plies with different geometries and creasing depths should be simulated. Moreover, different number of elements through the thickness should be considered to investigate the effect of mesh dependency. More specifically, the influence of the number of elements in the creasing and folding operation should be compared with the uniaxial tests. A length scale could be introduced in the modelling framework to reduce the localisation behaviour observed in the mesh study for the uniaxial tests.

Finally, the damage model could be extended so that also the folding of creased paperboard in the CD-direction is correctly predicted.

References

Biel, A., Tryding, J., Stigh, U., Ristinmaa, M., & Borgqvist, E. (2020). *Measurement of out-of-plane loaded paperboard in normal and shear direction* [unpublished].

Borgqvist, E. (2016). *Continuum modeling of the mechanical response of-paper-based materials.* (Doctoral dissertation). Lund University, Division of Solid mechanics. (ISBN:978-91-7623-665-9).

Borgqvist, E., Lindström, T., Tryding, J., Wallin, M., & Ristinmaa, M. (2014). Distortional hardening plasticity model for paperboard. *International Journal of Solids and Structures 51*, 2411–2423.

Calvin, S. I. (1988). The unique convertibility of paperboard. *Packaging technology and science Vol 1*, 77–92.

Coffin, D., & Nygårds, M. (2017). Creasing and folding. *Advances in Pulp and Paper Research, Oxford.*

Erhart, T., Bois, P. D., & Andrade, F. (2017). Short introduction of a new generalized damage model. *11th European LS-Dyna Conference.*

Harrysson, A., & Ristinmaa, M. (2008). Large strain elasto-plastic model of paper and corrugated board. *International Journal of Solids and Structures 45.*

Holzapfel, G. A. (2000). *Nonlinear solid mechanics.* John Wiley & Sons Ltd.

ISO:9895:2008. (2008). Paper and board– compressive strength – short-span test.

Livermore Software Technology. (2021). *LS-Dyna Keyword User's Manual, Volume II, Material Models.*

Nygårds, M. (2008). Experimental techniques for characterization of elasticplastic material properties in paperboard. *Nordic Pulp and Paper Research Journal Vol 23 no. 4/2008.*

Ristinmaa, M. (2020). *Introduction to non-linear finite element method* [unpublished course literature].

Ristinmaa, M., & Ottosen, N. S. (2008). *Introduction to large strain plasticity* [unpublished course literature].

Robertsson, K. (2018). *Integrating constitutive relations* [unpublished].

Robertsson, K. (2019). *Deriving stress tensor part 1, EB paper B* [unpublished].

Xia, Q. S., Boyce, M. C., & Parks, D. M. (2002). A constitutive model for the anisotropic elastic-plastic deformation of paper and paperboard. *International Journal of Solids and Structures 39*, 4053–4071.

7 Appendix

7.1 Large strain plasticity

In this section, some general background theory of large strain plasticity is provided. The notation convention in according to section 2.3.2. The most of the theory is based on the work done by Ristinmaa and Ottosen (2008). First, the basic principles of kinematics and thermodynamics are explained. Next, the EB material model is considered. The format of the free energy is specified and the stress tensor is derived.

7.1.1 Basic principles of kinematics

In this section, the basic principles of kinematics is explained. To shorten the explanation, only quantities relevant for understanding the considered material model is presented. To start with, it is stated that different configurations exist. In these, different descriptions are used. In the reference configuration, the coordinates X_i are called *material coordinates*, and the description is called the *Lagrangian description*. In the current configuration, the coordinates x_i are called *spatial coordinates*, and the description is called the *Eulerian description*. The change of a vector $d\boldsymbol{X}$ between two particles in the reference configuration to a vector $d\boldsymbol{x}$ between the same two particles in the current configuration is described by the *material deformation gradient tensor*

$$F_{ij} = \frac{\partial x_i}{\partial X_i}. \tag{19}$$

and the linear map is then given by

$$d\boldsymbol{x} = \boldsymbol{F} d\boldsymbol{X}.$$

To continue, it is stated that several different strain measures exist. The square of the distance between two particles in the current configuration is calculated as $ds^2 = (d\boldsymbol{x})^{\mathrm{T}} d\boldsymbol{x} = d\boldsymbol{X}^{\mathrm{T}} \boldsymbol{F}^{\mathrm{T}} \boldsymbol{F} d\boldsymbol{X}$. Here, the *right Cauchy-Green deformation tensor* is identified

$$\boldsymbol{C} = \boldsymbol{F}^{\mathrm{T}} \boldsymbol{F}.$$

Taking the difference $ds^2 - dS^2 = d\boldsymbol{X}^{\mathrm{T}} (\boldsymbol{F}^{\mathrm{T}} \boldsymbol{F} - \boldsymbol{I}) d\boldsymbol{X}$, the *Lagrangian strain tensor* is also identified

$$\boldsymbol{E} = \frac{1}{2}(\boldsymbol{F}^{\mathrm{T}} \boldsymbol{F} - \boldsymbol{I}) = \frac{1}{2}(\boldsymbol{C} - \boldsymbol{I}), \tag{20}$$

which allows the difference to be written as $ds^2 - dS^2 = 2 d\boldsymbol{X}^{\mathrm{T}} \boldsymbol{E} d\boldsymbol{X}$. Evidently, $\boldsymbol{E}$ is a symmetric second-order tensor. To obtain an expression for $ds^2 - dS^2$ expressed in derivatives with respect to the spatial coordinates, it is noted that it is possible to write $dS^2 = (d\boldsymbol{X})^{\mathrm{T}} d\boldsymbol{X} = d\boldsymbol{x}^{\mathrm{T}} \boldsymbol{F}^{-\mathrm{T}} \boldsymbol{F}^{-1} d\boldsymbol{x}$. Here, the *Cauchy's deformation tensor* is identified

$$\boldsymbol{c} = \boldsymbol{F}^{-\mathrm{T}} \boldsymbol{F}^{-1}.$$

Moreover, the *left Cauchy-Green deformation tensor*, or the *Finger's deformation tensor*, is introduced

$$\boldsymbol{b} = \boldsymbol{c}^{-1} = \boldsymbol{F} \boldsymbol{F}^{\mathrm{T}}.$$

It is noted that $\boldsymbol{C}$ is related to the reference configuration, whereas $\boldsymbol{b}$ is related to the current configuration. The use of uppercase and lowercase letters are in agreement

with the notation convention explained in section 2.3.2. These above introduced strain measures is sufficient for establishing the important relations needed to derive the EB elasto-plastic material model considered in this work. Hence, no more strain measures will be introduced. Next, the relationship between the volume and mass density in the reference and current configuration is established

$$\frac{dv}{dV} = \frac{\rho_o}{\rho} = \det\boldsymbol{F} = J,$$

where J is the Jacobian. Moreover, some time rate of change measures, instead of total strain measures, are introduced. These rate measures are useful when deriving the elasto-plastic material model. To start with, the *spatial velocity gradient* is defined as

$$l_{ij} = \frac{\partial v_i}{\partial x_j},$$

cf. Ristinmaa and Ottosen (2008) for a more extensive explanation. This quantity relates the material time derivative of the deformation gradient to the deformation gradient itself by

$$\dot{\boldsymbol{F}} = \boldsymbol{l}\boldsymbol{F}. \tag{21}$$

The spatial velocity gradient can be split into a symmetric and an antisymmetric part

$$\boldsymbol{l} = \frac{1}{2}(\boldsymbol{l} + \boldsymbol{l}^{\mathrm{T}}) + \frac{1}{2}(\boldsymbol{l} - \boldsymbol{l}^{\mathrm{T}}) = \boldsymbol{d} + \boldsymbol{w}, \tag{22}$$

where $\boldsymbol{d}$ is the *rate of deformation tensor* and $\boldsymbol{w}$ is the *spin tensor*.

The multiplicative split

Having introduced some important total strain and rate measures, the multiplicative split formulation is considered. The multiplicative split is a fundamental topic when considering large strain plasticity, and the reader is refereed to for example Holzapfel (2000) for a more detailed discussion. In the multiplicative split, the deformation gradient (19) is decomposed into an elastic and a plastic part. Previously it was stated that the mapping of a vector between two points in the reference configuration and the same two points in the current configuration is described as

$$d\boldsymbol{x} = \boldsymbol{F}d\boldsymbol{X}. \tag{23}$$

Now it is stated that the mapping of the vector goes via $d\bar{\boldsymbol{x}}$, i.e. an *intermediate configuration*. This mapping is described as

$$d\bar{\boldsymbol{x}} = \boldsymbol{F}^p d\boldsymbol{X}, \quad d\boldsymbol{x} = \boldsymbol{F}^e d\bar{\boldsymbol{x}}.$$

Hence, the total deformation is described as $d\boldsymbol{x} = \boldsymbol{F}^e d\bar{\boldsymbol{x}} = \boldsymbol{F}^e\boldsymbol{F}^p d\boldsymbol{X}$. Comparing this with (23) reveals that the deformation gradient is decomposed as

$$\boldsymbol{F} = \boldsymbol{F}^e\boldsymbol{F}^p, \tag{24}$$

where $\boldsymbol{F}^e$ and $\boldsymbol{F}^p$ are associated with the elastic and plastic deformation, respectively. The mapping of $d\boldsymbol{X}$ into the current configuration via the intermediate configuration is illustrated in Fig. 44. Consider now the Lagrangian strain tensor $\boldsymbol{E}$ introduced in

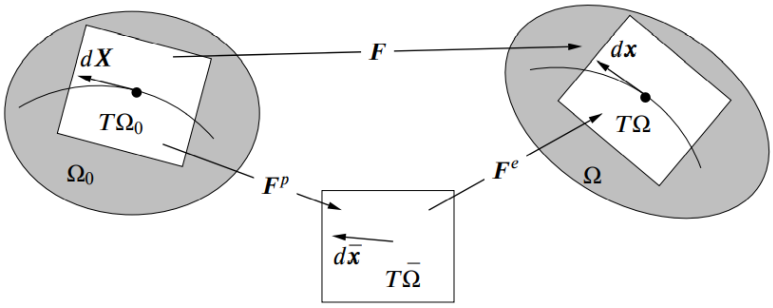

Figure 44: The mapping of the vector $d\boldsymbol{X}$ to the current configuration via the intermediate configuration by using the multiplicative split of the deformation gradient. Note that $T\boldsymbol{\Omega}_o$, $T\bar{\boldsymbol{\Omega}}$ and $T\boldsymbol{\Omega}$ represents the tangent spaces in the reference, intermediate and current configuration, respectively. Source: Ristinmaa and Ottosen (2008).

(20). Using (24) yields

$$\boldsymbol{E} = \frac{1}{2}(\boldsymbol{F}^{\mathrm{T}}\boldsymbol{F} - \boldsymbol{I}) = \frac{1}{2}(\boldsymbol{F}^{\mathrm{pT}}\boldsymbol{F}^{\mathrm{eT}}\boldsymbol{F}^{\mathrm{e}}\boldsymbol{F}^{\mathrm{p}} - \boldsymbol{I}). \tag{25}$$

Identifying the elastic and plastic strain tensors

$$\boldsymbol{E}^{\mathrm{e}} = \frac{1}{2}(\boldsymbol{C}^{\mathrm{e}} - \boldsymbol{I}), \quad \boldsymbol{C}^{\mathrm{e}} = \boldsymbol{F}^{\mathrm{eT}}\boldsymbol{F}^{\mathrm{e}},$$
$$\boldsymbol{E}^{\mathrm{p}}, = \frac{1}{2}(\boldsymbol{C}^{\mathrm{p}} - \boldsymbol{I}), \quad \boldsymbol{C}^{\mathrm{p}} = \boldsymbol{F}^{\mathrm{pT}}\boldsymbol{F}^{\mathrm{p}},$$

reveals that (25) can be rewritten as

$$\boldsymbol{E} = \boldsymbol{F}^{\mathrm{pT}}\boldsymbol{E}^{\mathrm{e}}\boldsymbol{F}^{\mathrm{p}} + \boldsymbol{E}^{\mathrm{p}}. \tag{26}$$

The conclusion of (26) is that the Lagrangian strain tensor $\boldsymbol{E}$ cannot be additive decomposed into an elastic and a plastic part, i.e. $\boldsymbol{E} \neq \boldsymbol{E}^{\mathrm{e}} + \boldsymbol{E}^{\mathrm{p}}$. It is noted that $\boldsymbol{E}^{\mathrm{e}}$ is a quantity defined in the intermediate configuration. To obtain a similar quantity related to the current configuration, the elastic Finger's deformation tensor is defined

$$\boldsymbol{b}^{\mathrm{e}} = \boldsymbol{F}^{\mathrm{e}}\boldsymbol{F}^{\mathrm{eT}}. \tag{27}$$

Taking the material derivative of the deformation gradient gives that

$$\dot{\boldsymbol{F}} = \dot{\boldsymbol{F}}^{\mathrm{e}}\boldsymbol{F}^{\mathrm{p}} + \boldsymbol{F}^{\mathrm{e}}\dot{\boldsymbol{F}}^{\mathrm{p}}. \tag{28}$$

Note now that the spatial velocity gradient according to (21) can be expressed as $\boldsymbol{l} = \dot{\boldsymbol{F}}\boldsymbol{F}^{\mathrm{p}-1}\boldsymbol{F}^{\mathrm{e}-1}$. Insertion of (28) into this yields

$$\boldsymbol{l} = \dot{\boldsymbol{F}}^{\mathrm{e}}\boldsymbol{F}^{\mathrm{e}-1} + \boldsymbol{F}^{\mathrm{e}}\dot{\boldsymbol{F}}^{\mathrm{p}}\boldsymbol{F}^{\mathrm{p}-1}\boldsymbol{F}^{\mathrm{e}-1}. \tag{29}$$

Introducing the *elastic velocity gradient*, $\boldsymbol{l}^{\mathrm{e}}$, the *material plastic velocity gradient*, $\boldsymbol{L}^{\mathrm{p}}$, and the *plastic velocity gradient*, $\boldsymbol{l}^{\mathrm{p}}$, as

$$\boldsymbol{l}^{\mathrm{e}} = \dot{\boldsymbol{F}}^{\mathrm{e}}\boldsymbol{F}^{\mathrm{e}-1}, \quad \boldsymbol{L}^{\mathrm{p}} = \dot{\boldsymbol{F}}^{\mathrm{p}}\boldsymbol{F}^{\mathrm{p}-1}, \quad \boldsymbol{l}^{\mathrm{p}} = \boldsymbol{F}^{\mathrm{e}}\boldsymbol{L}^{\mathrm{p}}\boldsymbol{F}^{\mathrm{e}-1}, \tag{30}$$

yields that (29) can be written as

$$\boldsymbol{l} = \boldsymbol{l}^{\mathrm{e}} + \boldsymbol{l}^{\mathrm{p}}. \tag{31}$$

Splitting the substructure

In a continuum material model, i.e. in a model assuming that the microscopic structure and behaviour of a material can be described on a larger, macroscopic level, some preferred directions normally exists in the material. This is certainly the case for the paperboard material which the main directions are the MD-, CD- and ZD-direction. Hence, the material can be viewed as orthotropic, i.e. to possess three fundamental symmetry planes. The directions describing these planes are called *material directions*, denoted $\boldsymbol{v}^{(\alpha)}$, where $\alpha \in (1,2,3)$. The material directions are denoted $\boldsymbol{v}_o^{(\alpha)}$, $\bar{\boldsymbol{v}}^{(\alpha)}$ and $\boldsymbol{v}^{(\alpha)}$ in the reference, intermediate and current configuration, respectively. The directions describes the *substructure* of the material. In the establishment of the anisotropic theory, the material directions are during the deformation allowed to evolve. Analogous to the deformation gradient, describing the relationship between the current configuration and the reference configuration, refer to (23), there exists a mapping of the material directions

$$\boldsymbol{v}^{(\alpha)} = \boldsymbol{\Delta}^{(\alpha)} \boldsymbol{v}_o^{(\alpha)},$$

where the map $\boldsymbol{\Delta}^{(\alpha)}$ is assumed as

$$\boldsymbol{\Delta}^{(\alpha)} = \boldsymbol{\beta}^{(\alpha)} \boldsymbol{\alpha}^{(\alpha)}.$$

As illustrated in Fig. 45, the mapping from the reference configuration to the inter-

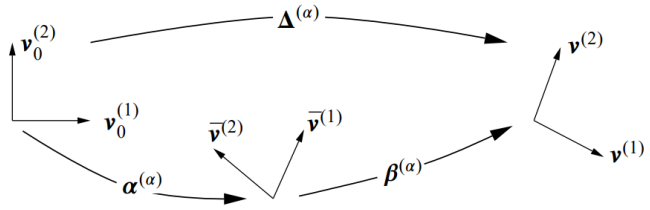

Figure 45: The mapping of the substructure via the intermediate configuration. Source: Ristinmaa and Ottosen (2008).

mediate configuration and from the intermediate configuration to the current configuration is thus expressed as

$$\bar{\boldsymbol{v}}^{(\alpha)} = \boldsymbol{\alpha}^{(\alpha)} \boldsymbol{v}_o^{(\alpha)}, \tag{32}$$

$$\boldsymbol{v}^{(\alpha)} = \boldsymbol{\beta}^{(\alpha)} \bar{\boldsymbol{v}}^{(\alpha)}. \tag{33}$$

It is preferred that, if only elastic deformations take place, the substructure and the continuum deforms in a uniform manner. This constitutive assumption can be expressed as

$$\boldsymbol{\beta}^{(\alpha)} = \boldsymbol{F}^{\mathrm{e}}.$$

It is stated that the intermediate configuration is not uniquely given. Thus, it must be specified. Moreover, the evolution of the material director vectors must also be specified. Finally, it is noted that if $\boldsymbol{v}^{(\alpha)}$ is a material direction, then $-\boldsymbol{v}^{(\alpha)}$ is also a material direction. To take this into account, an equal number of *structural tensors* $\boldsymbol{m}^{(\alpha)}$ are defined as $\boldsymbol{m}^{(\alpha)} = \boldsymbol{v}^{(\alpha)} \otimes \boldsymbol{v}^{(\alpha)}$.

For the EB elasto-plastic material model the intermediate configuration is chosen to be *isoclinic*, refer to Borgqvist (2016). This means that the material directions in the intermediate configuration are aligned with the material directions in the reference configuration, i.e. that $\boldsymbol{\alpha}^{(\alpha)} = \boldsymbol{I}$, compare with (32). Thus, from (33) it is evident that the material directions become

$$\boldsymbol{v}^{(\alpha)} = \boldsymbol{F}^{\mathrm{e}}\boldsymbol{v}_o^{(\alpha)}.$$

However, according to Borgqvist (2016), the third, out-of-plane material direction is chosen somewhat different, namely as the normal to the plane given by the two in-plane direction vectors. The normal direction is obtained by taking the cross-product of these two in-plane vectors. The three direction vectors can then be summarized as

$$\boldsymbol{v}^{(1)} = \boldsymbol{F}^{\mathrm{e}}\boldsymbol{v}_o^{(1)}, \quad \boldsymbol{v}^{(2)} = \boldsymbol{F}^{\mathrm{e}}\boldsymbol{v}_o^{(2)}, \quad \boldsymbol{n}^{(3)} = \boldsymbol{v}^{(1)} \times \boldsymbol{v}^{(2)} = \sqrt{\det(\boldsymbol{b}^{\mathrm{e}})}\boldsymbol{F}^{\mathrm{e-T}}\boldsymbol{n}_o^{(3)},$$

with the corresponding structural tensors given by

$$\boldsymbol{m}^{(1)} = \boldsymbol{v}^{(1)} \otimes \boldsymbol{v}^{(1)}, \quad \boldsymbol{m}^{(2)} = \boldsymbol{v}^{(2)} \otimes \boldsymbol{v}^{(2)}, \quad \boldsymbol{m}^{(3)} = \boldsymbol{n}^{(3)} \otimes \boldsymbol{n}^{(3)}. \tag{34}$$

Finally, it is once again underlined that the third, not used, material direction $\boldsymbol{v}^{(3)} = \boldsymbol{F}^{\mathrm{e}}\boldsymbol{v}_o^{(3)}$ is not perpendicular to the in-plane vectors, i.e. $\boldsymbol{v}^{(3)} \cdot \boldsymbol{v}^{(1)} \neq 0$. Hence, this vector has components in the MD-direction. By using the normal $\boldsymbol{n}^{(3)}$ instead of $\boldsymbol{v}^{(3)}$, the in-plane and out-of-plane coupling is reduced. Using a more reduced coupling between the in-plane and out-of-plane properties is confirmed by experimental testing, refer to Figs. 2 and 3.

7.1.2 Basic principles of thermodynamics

The purpose of this section is to give a background of the thermodynamic framework of which the elasto-plastic material model is derived. However, the basic principles of thermodynamics will only be explained in a concise manner. The explanations and derivations are done with the aim of retrieving a formulation suitable for the purpose of constitutive modeling. To start with, the concept of absolute temperature is stated

$$\theta > 0 \text{ absolute temperature},$$

i.e. if the lowest value of the temperature measure is zero, the temperature is said to be absolute Ristinmaa and Ottosen (2008). Next, it is mentioned that *state variables* are variables that characterize the state of a system, whereas *state functions* are functions only depending on the current state. The first law of thermodynamics states that the mechanical work created by a machine during one cycle cannot be larger than what is absorbed as heat. Now, the global and local form of the first law of thermodynamics are to be stated. However, the rate of mechanical work and heat input must first be formulated. Considering a body in its deformed configuration, the rate of mechanical work input can be stated as

$$\frac{\delta W}{dt} = \int_s v_i t_i \, \mathrm{d}s + \int_v \rho v_i b_i \, \mathrm{d}v,$$

where $\frac{\delta W}{dt}$ is the rate of the mechanical work input, ρ is the density in the deformed configuration, t_i the traction vector, b_i the body force and v_i the velocity. Similarly,

the rate of heat input can be stated as

$$\frac{\delta Q}{dt} = \int_v \rho r \, \mathrm{d}v - \int_s q_i n_i \, \mathrm{d}s,$$

where r is the body heat supply per unit time and unit mass and n_i is the unit normal vector. The kinetic energy is given by

$$K = \frac{1}{2} \int_v \rho v_i v_i \, \mathrm{d}v,$$

which is evidently a state function Ristinmaa and Ottosen (2008). The time material derivative of this is

$$\frac{DK}{Dt} = \int_v \rho a_i v_i \, \mathrm{d}v,$$

where a_i denotes the acceleration. Now it is possible to state *the global form of the first law of thermodynamics*

$$\frac{DK}{Dt} + \frac{DU}{Dt} = \frac{\delta W}{dt} + \frac{\delta Q}{dt}.$$

Here, U is the internal energy of the system. By introducing the specific internal energy, u, and taking advantage of Gauss's divergence theorem, it is possible to retrieve *the local form of the first law*

$$\rho \frac{Du}{Dt} = d_{ij}\sigma_{ij} + \rho r - q_{i,i}.$$

The second law of thermodynamics states that during a cycle, a machine cannot produce mechanical work completely equal to the heat supplied from one reservoir. Introducing the entropy S, as well as the specific entropy s, it is possible to state *the global form of the second law*

$$\frac{DS}{Dt} \geq \int_v \rho \frac{r}{\theta} \, \mathrm{d}v - \int_s \frac{q_i}{\theta} n_i \, \mathrm{d}s,$$

which is also called the *Clausius-Duhem inequality*. From this, it is possible to derive *the local form of the second law*

$$\rho \frac{Ds}{Dt} - \rho \frac{r}{\theta} + \frac{1}{\theta} q_{i,i} - \frac{1}{\theta^2} q_i \theta_{,i} \geq 0,$$

cf. Ristinmaa and Ottosen (2008). Eliminating the term $q_{i,i} - \rho r$ from the local form of the first law, this law can be rewritten as

$$\gamma = \theta \rho \frac{Ds}{Dt} + d_{ij}\sigma_{ij} - \rho \frac{Du}{Dt} - \frac{q_i \theta_{,i}}{\theta} \geq 0.$$

This equation is called the *dissipation inequality*. It is noted that the equal sign holds if the process is reversible whereas the inequality sign holds if the process is irreversible. It is emphasized that if the constitutive model fulfills the dissipation inequality, it also fulfills all thermodynamic requirements. If noted that both the specific internal energy, u, as well as the specific entropy, s, are state functions, it is possible to introduce a third state function, namely the *Helmholz' free energy per unit mass*, ψ, defined as

$$\psi = u - s\theta.$$

The dissipation inequality can then be rewritten in terms of the Helmholz' free energy

$$\gamma = -\rho\Big(\frac{D\psi}{Dt} + s\frac{D\theta}{Dt}\Big) + d_{ij}\sigma_{ij} - \frac{1}{\theta}q_i\theta_{,i} \geq 0.$$

For isothermal conditions, reformulated to the reference configuration, this reads

$$\gamma_o = \boldsymbol{\tau} : \boldsymbol{d} - \rho_o\dot{\psi} \geq 0, \tag{35}$$

where $\boldsymbol{\tau}$ is the Kirchhoff stress tensor and $\boldsymbol{d}$ is the rate of deformation tensor. In the reference configuration, the Kirchhoff stress tensor and the rate of deformation tensor are energy conjugated quantities, refer to Ristinmaa (2020).

7.1.3 Derivation of the stress tensor

In this section, the stress tensor of the EB material model is derived. The derivation starts by considering the just derived dissipation inequality (35). As previously stated, if this equation is fulfilled, then all formal requirements provided by thermodynamics are fulfilled. To formulate the material model, the free energy must be specified. It is assumed that the free energy can be additively split into an elastic and a plastic part, cf. Ristinmaa and Ottosen (2008) and Borgqvist (2016). For the EB material model, the free energy is chosen as

$$\psi = \psi^e(\boldsymbol{b}^e, \boldsymbol{m}^{(\alpha)}) + \psi^p(\kappa^{(\gamma)}),$$

cf. Borgqvist (2016). The dissipation inequality (35) can then be formulated as

$$\gamma_o = \boldsymbol{\tau} : \boldsymbol{d} - \rho_o\frac{\partial\psi^e}{\partial\boldsymbol{b}^e} : \dot{\boldsymbol{b}}^e - \sum\rho_o\frac{\partial\psi^{\mathrm{e}}}{\partial\boldsymbol{m}^{(\alpha)}} : \dot{\boldsymbol{m}}^{(\alpha)} - K\dot{\kappa}^{(\gamma)} \geq 0, \tag{36}$$

where the conjugated thermodynamic forces is identified as

$$K^{(\gamma)} = \rho_o\frac{\partial\psi^p}{\partial\kappa^{(\gamma)}}.$$

To proceed, the material derivative of the elastic Finger's deformation tensor (27) is calculated as

$$\begin{aligned}\dot{\boldsymbol{b}}^e &= \dot{\boldsymbol{F}}^e\boldsymbol{F}^{\mathrm{eT}} + \boldsymbol{F}^{\mathrm{e}}\dot{\boldsymbol{F}}^{\mathrm{eT}} = \dot{\boldsymbol{F}}^{\mathrm{e}}\boldsymbol{F}^{\mathrm{e}-1}\boldsymbol{F}^{\mathrm{e}}\boldsymbol{F}^{\mathrm{eT}} + \boldsymbol{F}^{\mathrm{e}}\boldsymbol{F}^{\mathrm{eT}}\boldsymbol{F}^{\mathrm{e}-\mathrm{T}}\dot{\boldsymbol{F}}^{\mathrm{eT}} = \boldsymbol{l}^{\mathrm{e}}\boldsymbol{b}^{\mathrm{e}} + \boldsymbol{b}^{\mathrm{e}}\boldsymbol{l}^{\mathrm{eT}} \\ &= \boldsymbol{l}^{\mathrm{e}}\boldsymbol{b}^{\mathrm{e}} + (\boldsymbol{l}^{\mathrm{e}}\boldsymbol{b}^{\mathrm{e}})^{\mathrm{T}} = 2\mathrm{sym}(\boldsymbol{l}^{\mathrm{e}}\boldsymbol{b}^{\mathrm{e}}),\end{aligned} \tag{37}$$

where $\boldsymbol{l}^{\mathrm{e}}$ was defined in (30) and it is noted that $\boldsymbol{b}^{\mathrm{e}}$ is a symmetric tensor. Moreover, the material derivative of the first structural tensor is calculated as

$$\begin{aligned}\dot{\boldsymbol{m}}^{(1)} &= \dot{\boldsymbol{v}}^{(1)}\otimes\boldsymbol{v}^{(1)} + \boldsymbol{v}^{(1)}\otimes\dot{\boldsymbol{v}}^{(1)} = \big[\dot{\boldsymbol{v}}^{(1)} = \dot{\overline{\boldsymbol{F}^{\mathrm{e}}\boldsymbol{v}_o^{(1)}}} = \dot{\boldsymbol{F}}^{\mathrm{e}}\boldsymbol{v}_o^{(1)} = \boldsymbol{l}^{\mathrm{e}}\boldsymbol{F}^{\mathrm{e}}\boldsymbol{v}_o^{(1)} = \boldsymbol{l}^{\mathrm{e}}\boldsymbol{v}^{(1)}\big] \\ &= \boldsymbol{l}^{\mathrm{e}}\boldsymbol{v}^{(1)}\boldsymbol{v}^{(1)\mathrm{T}} + \boldsymbol{v}^{(1)}(\boldsymbol{l}^{\mathrm{e}}\boldsymbol{v}^{(1)})^{\mathrm{T}} = \boldsymbol{l}^{\mathrm{e}}\boldsymbol{m}^{(1)} + \boldsymbol{m}^{(1)}\boldsymbol{l}^{\mathrm{eT}} = 2\mathrm{sym}(\boldsymbol{l}^{\mathrm{e}}\boldsymbol{m}^{(1)}),\end{aligned} \tag{38}$$

where it was used that $\boldsymbol{m}^{(1)}$ is a symmetric tensor. The material derivative of the second structural tensor is obtained in the exact same manner

$$\dot{\boldsymbol{m}}^{(2)} = 2\mathrm{sym}(\boldsymbol{l}^{\mathrm{e}}\boldsymbol{m}^{(2)}). \tag{39}$$

The material derivative of the third structural tensor is calculated as

$$\dot{\boldsymbol{m}}^{(3)} = 2\mathrm{tr}(\boldsymbol{l}^{\mathrm{e}})\boldsymbol{m}^{(3)} - 2\mathrm{sym}(\boldsymbol{l}^{\mathrm{eT}}\boldsymbol{m}^{(3)}), \tag{40}$$

refer to Robertsson (2019) for a complete derivation. Insertion of (37), (38), (39) and (40) into the dissipation inequality (36) yields

$$\gamma_o = \boldsymbol{\tau} : \boldsymbol{d} - 2\rho_o \frac{\partial \psi^e}{\partial \boldsymbol{b}^e} : \mathrm{sym}(\boldsymbol{l}^e \boldsymbol{b}^e) - 2\rho_o \frac{\partial \psi^e}{\partial \boldsymbol{m}^{(1)}} : \mathrm{sym}(\boldsymbol{l}^{\mathrm{e}} \boldsymbol{m}^{(1)}) - 2\rho_o \frac{\partial \psi^e}{\partial \boldsymbol{m}^{(2)}} : \mathrm{sym}(\boldsymbol{l}^e \boldsymbol{m}^{(2)})$$

$$- 2\rho_o \frac{\partial \psi^e}{\partial \boldsymbol{m}^{(3)}} : (\mathrm{tr}(\boldsymbol{l}^{\mathrm{e}})\boldsymbol{m}^{(3)}) + 2\rho_o \frac{\partial \psi^e}{\partial \boldsymbol{m}^{(3)}} : \mathrm{sym}(\boldsymbol{l}^{\mathrm{eT}} \boldsymbol{m}^{(3)}) - K\dot{\kappa}^{(\gamma)} \geq 0. \tag{41}$$

It is noted that given a symmetric tensor $\boldsymbol{A} = \boldsymbol{A}^{\mathrm{T}}$ the following relations hold

$$\begin{aligned}
\frac{\partial \psi^e}{\partial \boldsymbol{A}} : \mathrm{sym}(\boldsymbol{l}^{\mathrm{e}} \boldsymbol{A}) &= \frac{\partial \psi^e}{\partial \boldsymbol{A}} \boldsymbol{A} : \boldsymbol{l}^{\mathrm{e}} \\
\frac{\partial \psi^e}{\partial \boldsymbol{A}} : \mathrm{sym}(\boldsymbol{l}^{\mathrm{eT}} \boldsymbol{A}) &= \boldsymbol{A} \frac{\partial \psi^e}{\partial \boldsymbol{A}} : \boldsymbol{l}^{\mathrm{e}} \\
\frac{\partial \psi^e}{\partial \boldsymbol{m}^{(3)}} : (\mathrm{tr}(\boldsymbol{l}^{\mathrm{e}})\boldsymbol{m}^{(3)}) &= \Big(\frac{\partial \psi^e}{\partial \boldsymbol{m}^{(3)}} : \boldsymbol{m}^{(3)} \Big) \boldsymbol{I} : \boldsymbol{l}^{\mathrm{e}},
\end{aligned}$$

cf. Robertsson (2019). Using the above relations, as well as the fact that $\boldsymbol{l}^{\mathrm{e}} = \boldsymbol{l} - \boldsymbol{l}^{\mathrm{p}}$ according to (31), the dissipation inequality (41) can be reformulated as

$$\gamma_o = \boldsymbol{\tau} : \boldsymbol{d} - 2\rho_o \Big(\frac{\partial \psi^e}{\partial \boldsymbol{b}^e} \boldsymbol{b}^{\mathrm{e}} + \frac{\partial \psi^e}{\partial \boldsymbol{m}^{(1)}} \boldsymbol{m}^{(1)} + \frac{\partial \psi^e}{\partial \boldsymbol{m}^{(2)}} \boldsymbol{m}^{(2)} - \boldsymbol{m}^{(3)} \frac{\partial \psi^e}{\partial \boldsymbol{m}^{(3)}} + \Big(\frac{\partial \psi^e}{\partial \boldsymbol{m}^{(3)}} : \boldsymbol{m}^{(3)} \Big) \boldsymbol{I} \Big) : \boldsymbol{l}$$

$$+ 2\rho_o \Big(\frac{\partial \psi^e}{\partial \boldsymbol{b}^e} \boldsymbol{b}^{\mathrm{e}} + \frac{\partial \psi^e}{\partial \boldsymbol{m}^{(1)}} \boldsymbol{m}^{(1)} + \frac{\partial \psi^e}{\partial \boldsymbol{m}^{(2)}} \boldsymbol{m}^{(2)} - \boldsymbol{m}^{(3)} \frac{\partial \psi^e}{\partial \boldsymbol{m}^{(3)}} + \Big(\frac{\partial \psi^e}{\partial \boldsymbol{m}^{(3)}} : \boldsymbol{m}^{(3)} \Big) \boldsymbol{I} \Big) : \boldsymbol{l}^{\mathrm{p}}$$
$$- K\dot{\kappa}^{(\gamma)} \geq 0.$$

Now it is noted that the expression inside the parenthesis is symmetric. Thus, by decomposing the spatial velocity gradient according to (22), i.e. as $\boldsymbol{l} = \boldsymbol{d} + \boldsymbol{w}$, as well as $\boldsymbol{l}^{\mathrm{p}} = \boldsymbol{d}^{\mathrm{p}} + \boldsymbol{w}^{\mathrm{p}}$, the following is obtained

$$\gamma_o = \Big(\boldsymbol{\tau} - 2\rho_o \Big(\frac{\partial \psi^e}{\partial \boldsymbol{b}^e} \boldsymbol{b}^{\mathrm{e}} + \frac{\partial \psi^e}{\partial \boldsymbol{m}^{(1)}} \boldsymbol{m}^{(1)} + \frac{\partial \psi^e}{\partial \boldsymbol{m}^{(2)}} \boldsymbol{m}^{(2)} - \boldsymbol{m}^{(3)} \frac{\partial \psi^e}{\partial \boldsymbol{m}^{(3)}} + \Big(\frac{\partial \psi^e}{\partial \boldsymbol{m}^{(3)}} : \boldsymbol{m}^{(3)} \Big) \boldsymbol{I} \Big) \Big) : \boldsymbol{d}$$

$$+ 2\rho_o \Big(\frac{\partial \psi^e}{\partial \boldsymbol{b}^e} \boldsymbol{b}^{\mathrm{e}} + \frac{\partial \psi^e}{\partial \boldsymbol{m}^{(1)}} \boldsymbol{m}^{(1)} + \frac{\partial \psi^e}{\partial \boldsymbol{m}^{(2)}} \boldsymbol{m}^{(2)} - \boldsymbol{m}^{(3)} \frac{\partial \psi^e}{\partial \boldsymbol{m}^{(3)}} + \Big(\frac{\partial \psi^e}{\partial \boldsymbol{m}^{(3)}} : \boldsymbol{m}^{(3)} \Big) \boldsymbol{I} \Big) : \boldsymbol{d}^{\mathrm{p}}$$

$$- K\dot{\kappa}^{(\gamma)} \geq 0. \tag{42}$$

As the dissipation inequality should hold for any values of $\boldsymbol{d}$, the Kirchhoff stress tensor is identified as

$$\boldsymbol{\tau} = 2\rho_o \Big(\frac{\partial \psi^e}{\partial \boldsymbol{b}^e} \boldsymbol{b}^{\mathrm{e}} + \frac{\partial \psi^e}{\partial \boldsymbol{m}^{(1)}} \boldsymbol{m}^{(1)} + \frac{\partial \psi^e}{\partial \boldsymbol{m}^{(2)}} \boldsymbol{m}^{(2)} - \boldsymbol{m}^{(3)} \frac{\partial \psi^e}{\partial \boldsymbol{m}^{(3)}} + \Big(\frac{\partial \psi^e}{\partial \boldsymbol{m}^{(3)}} : \boldsymbol{m}^{(3)} \Big) \boldsymbol{I} \Big).$$

The dissipation inequality (42) thus reduces to

$$\gamma_o = \boldsymbol{\tau} : \boldsymbol{d}^p - K\dot{\kappa}^{(\gamma)} \geq 0.$$

7.2 Calculating the pretension displacement

In this section, the choice of the pretension displacement used in the line creasing operation is described. With the elastic part of the free energy established it is possible to calculate the initial tangent stiffness. The initial stiffness can be calculated as

$$\mathbb{D}_{initial} = \frac{\partial \boldsymbol{\tau}}{\partial \boldsymbol{F}^e} \boldsymbol{F}^{eT}|_{\boldsymbol{F}^e = \boldsymbol{I}},$$

cf. Ristinmaa and Ottosen (2008). With the chosen free energy (3), the initial constitutive equation, using Voigt notation is written

$$\begin{bmatrix} \sigma_{11} \\ \sigma_{22} \\ \sigma_{33} \\ \sigma_{12} \\ \sigma_{13} \\ \sigma_{23} \end{bmatrix} = \begin{bmatrix} 2A_1 + 2A_4 & A_4 & & & & \\ A_4 & 2A_2 + 2A_4 & & & & \\ & & 2H^+A_3 + 4(1-H^+)A_6A_7 & & & \\ & & & A_4 + A_5 & & \\ & & & & A_5 & \\ & & & & & A_5 \end{bmatrix} \begin{bmatrix} \varepsilon_{11} \\ \varepsilon_{22} \\ \varepsilon_{33} \\ \varepsilon_{12} \\ \varepsilon_{13} \\ \varepsilon_{23} \end{bmatrix},$$

cf. Borgqvist (2016). Note that blank entities represents zero. It is observed that the pretension displacement is giving rise to a state of plane strain as the only non-zero component of the strain tensor is the strain in the MD-direction, ε_{11}. This strain can thus easily be calculated as

$$\varepsilon_{11} = \frac{\sigma_{11}}{2(A_1 + A_4)}.$$

As the initial pretension force is supposed to be 58 N, and the width is 38 mm and the thickness is 0.39 mm, the stress σ_{11} is calculated to

$$\sigma_{11} = \frac{58}{0.39 \cdot 38} = 3.91 \text{ MPa}.$$

The in-plane elastic material parameters are for the paperboard material calibrated to $A_1 = 1721$ MPa and $A_4 = 1263$ MPa, cf. Table 2. Thus, the strain is calculated to

$$\varepsilon_{11} = \frac{3.91}{2(1721 + 1263)} = 6.56 \cdot 10^{-4}.$$

Since the paperboard in the line creasing method is 110 mm long, the prescribed pretension displacement u_w, compare with Fig. 5, is for each side of the specimen calculated to

$$u_w = \varepsilon_{11} \cdot \frac{110}{2} = 6.56 \cdot 10^{-4} \cdot \frac{110}{2} = 0.036 \text{ mm}.$$